Boosting photocatalytic degradation of estrone hormone by silica-supported g-C3N4/WO3 using response surface methodology coupled with Box-Behnken design

Citation

ALI, Hassan, Muhammad YASIR, Fahanwi ASABUWA NGWABEBHOH, Tomáš ŠOPÍK, Oyunchimeg ZANDRAA, Jakub ŠEVČÍK, Milan MASAŘ, Michal MACHOVSKÝ, and Ivo KUŘITKA. Boosting photocatalytic degradation of estrone hormone by silica-supported g-C3N4/WO3 using response surface methodology coupled with Box-Behnken design. *Journal of Photochemistry and Photobiology A: Chemistry* [online]. vol. 441, Elsevier, 2023, [cit. 2024-10-29]. ISSN 1010-6030. Available at https://www.sciencedirect.com/science/article/pii/S1010603023001983

DOI

https://doi.org/10.1016/j.jphotochem.2023.114733

Permanent link

https://publikace.k.utb.cz/handle/10563/1011494

Boosting photocatalytic degradation of estrone hormone by silica-supported g-C_3N_4/WO_3 using response surface methodology coupled with Box-Behnken design

Hassan Ali, Muhammad Yasir, Fahanwi Asabuwa Ngwabebhoh, Tomas Sopik, Oyunchimeg Zandraa, Jakub Sevcik, Milan Masar, Michal Machovsky*, Ivo Kuritka

Centre of Polymer Systems, Tomas Bata University in Zlin, tr. T. Bati 5678, 760 01 Zlin, Czech Republic

*Corresponding author. E-mail address: machovsky@utb.cz (M. Machovsky).

ABSTRACT

In this article, we report on the preparation and characterization of silica-supported g-C_3N_4/WO_3 nanocomposite with boosted photocatalytic performance towards the degradation of estrone hormone by using response surface methodology (RSM) coupled with the Box-Behnken model to determine the synergistic effects of three independent experimental parameters (hormone concentration, solution pH, and photocatalyst dosage). The RSM results were consistent with the prediction model ($R^2 > 0.958$ and 0.934 for UV and visible light irradiation, respectively). The optimized experimental test conditions were evaluated as follows: 3000 μg of photocatalyst dosage, 300 μg/L of hormone concentration, and pH 7. The hormone photodegradation efficiencies under these experimental parameters were 100% and 96% after 3 h of UV and visible light irradiation, respectively. Additionally, degradation kinetics (first-order, second-order, and intraparticle diffusion model), adsorption isotherms (Freundlich and Langmuir), and antibacterial activity of the prepared sample were also examined. Radical scavenging tests were performed to elucidate the photodegradation mechanism and the existence of reactive oxygen species. The recyclability test showed that the efficiency remained above 75% after seven consecutive cycles. The results indicate that the RSM based on the Box-Behnken model is an excellent approach for determining optimized experimental parameters for specific degradation of estrogenic hormones.

Keywords: Photocatalysis, g-C_3N/WO_3, estrone degradation, response surface methodology, Box-Behnken design, kinetics

1. Introduction

Rapid industrialization and human population growth over several decades have led to a rise in various environmental issues, such as climate change, air pollution, ocean acidification, and water pollution. As a result, numerous environmental toxicants in everyday household items have been identified that pose acute risks to humans and animals alike. These synthetic chemicals constitute a range of broadly categorized chemicals such as endocrine disrupting chemicals ($EDCs$), per-fluoroalkyl and polyfluoroalkyl substances ($PFAS$), and contaminants of emerging concern (CECs) [**1**]. These environmental pollutants are quite persistent, and their remediation remains a critical issue to be addressed. The problem is further exacerbated as those pollutants interfere with the normal neurological and hormonal balance in animals and have been implicated in various diseases such as cancer, diabetes, and heart disease in humans [**2-4**]. Among these pollutants, synthetically and naturally produced hormones such as estrone ($E1$) have been detected at elevated concentrations throughout the natural water sources prompting various environmental regulatory agencies to establish a threshold limit for these toxicants [**5**]. In regard to the elimination of these toxic chemicals, several techniques have been employed so far, such as membrane technology, nanofibers, ozonation, and photocatalysis [**6-10**].

To date, photocatalysis is considered one of the most attractive approaches for various environmental and energy applications, including hazardous pollutants removal, mainly due to relatively low energy-cost requirements as well as minimized secondary pollution [**11-14**]. The concept of photocatalysis has been around for decades as the first and extensively reported photocatalyst, titanium dioxide (TiO_2), is still considered attractive due to its efficiency and chemical stability [**15**]. However, there are a few drawbacks associated with the most commonly investigated photocatalysts, i.e., (i) intrinsic poor visible light harvesting due to large bandgap, (ii) rapid charge recombination without participation in redox reactions, and (iii) chemical stability [**16**]. Several strategies have been investigated to address these common drawbacks associated with single-component photocatalysts resulting in poor efficiencies, such as metal doping, defect engineering, band engineering, vacancies engineering, employing metal-organic frameworks (MOFs), and formation of a suitable heterojunction [**17-20**]. Hybrid photocatalysts based on staggered bandgap configuration have garnered much attention over the last few years due to their advantageous charge mechanism in comparison to single-component photocatalysts. As in the case of dual-component photocatalysts, the enhanced charge carriers pathway results in the preservation of charge species of the conduction band (CB) and valence band (VB) with high redox potential [**21**]. However, the successful construction of a heterostructured photocatalyst entails the careful selection of individual components. In this regard, the relative energy band positions should fulfill the criterion, i. e., an oxidizing component with a minimum VB position at 1.23 V and a reducing component with a minimum CB position at 0 V (NHE scale). For organic hormones degradation, a single component with a higher oxidizing potential, i.e., a more positive VB potential, is desired for generating reactive oxygen species (ROS). These ROS, along with holes (h^+) and superoxide anions ($O_2^{\bullet}$) collectively contribute towards photocatalytic degradation [**22**]. So far, various types of photocatalytic materials have been extensively investigated such as TiO_2, ZnO, WO_3, and their nanocomposites [**23-25**]. Among reported heterostructures, polymeric graphitic carbon nitride (g-C_3N_4) and tungsten trioxide (WO_3) have gained much attention due to their relatively suitable optoelectronic properties, structural stability, and visible light photoactivity owing to a smaller bandgap [**26**]. Furthermore, an attractive combination is obtained since the band-edge positions of g-C_3N_4 and WO_3 are highly reducing and oxidizing, respectively, due to their corresponding CB and VB. It is pertinent to mention here that WO_3 itself is insufficient for organic pollutants degradation due to the low CB potential required for the single-electron reduction of molecular O2. Therefore, it has to be decorated by noble metals such as Ag or Pt or coupled with a reductive semiconductor to achieve a feasible photocatalytic redox potential [**27**]. Moreover, constructed photocatalysts are usually supported by inert materials such as silica, alumina, and zeolites to impart thermal and chemical stability. In a nutshell, for constructing a hybrid photocatalytic system, g-C3N_4/WO_3 presents an attractive combination as WO_3 and g-C_3N_4 possess sufficient redox potential to act as oxidation and reduction components, respectively. g-C_3N_4 has already been employed in various photocatalytic applications in single and tandem heterostructured assemblies, such as dye degradation, CO_2 reduction, indoor air purification, dehydrogenation, and hydrogen production [**28-32**].

From the proceeding discussion, it is clear that the photocatalytic degradation process is primarily dependent on optoelectronics properties. Besides that, other operational parameters such as solution pH, pollutant concentration, and photocatalyst dose also greatly influence the efficiency of a specific system [**33**]. Therefore, in the context of the commercial applicability of photocatalysts, it is imperative to develop an experimental design for the optimization of variable experimental factors. Response surface methodology (RSM) has been widely used to optimize various processes, including photocatalysis in which the influence of selected factors on the response process (photocatalytic degradation) is examined, and reliable conclusions about a specific system can be drawn [**34**]. Numerous literature studies exist using RSM for the optimization of photocatalytic reactors [**35-37**]. The most commonly used experimental designs are central composite design (CCD), artificial neural networks (ANN), Box-Behnken design (BBD), and Doehlert matrix (DM) for the optimization of photocatalytic processes [**38-45**]. However, it has been suggested the BBD model offers more suitability in wastewater treatment applications due to fewer experimental runs required to perform and thereby saving energy, cost, and time [**46**].

So far, to the best of our knowledge, no study has been conducted on the optimization and modeling of silica-supported g-C_3N_4/WO_3 for the degradation of estrogenic hormones, particularly $E1$. In this paper, we report on the optimization of photocatalytic degradation of silicasupported g-C3N_4/WO_3 using three selected independent variable operational parameters, i.e., pH, photocatalyst dosage, and $E1$ hormone concentration via RSM and demonstrate its application feasibility for boosting photocatalytic driven degradation of estrogenic hormones under UV and visible light irradiation. BBD experimental design model is used to obtain optimized experimental conditions. Moreover, degradation kinetics, adsorption isotherms, and antibacterial properties of the as-prepared nanocomposite are also evaluated. Lastly, a radical scavenging test was performed to elucidate the charge transfer mechanism. The feasibility of the nanocomposite from a practical point of view was also evaluated using a seven-cyclic reusability study.

2. Experimental

2.1. Materials

Hydrophilic fumed silica (Orisil 200), Urea (ReagentPlus ≥ 99.5%, Sigma-Aldrich) ammonia (ammonium hydroxide solution 25%, p.a., Lach-Ner), and tungstic acid (99%, Sigma-Aldrich) were used as received for material synthesis. The hormone solution was prepared by estrogenic hormone ($E1$) $\geq$ 99% sourced from Sigma Aldrich Chemie GmbH, Germany. Filters with pores size of 0.45 μm and 25 mm in width were provided by Whatman, Czech Republic for the collection of aliquots. Deionized water was used throughout the experiments obtained from the Milli-Q water purifier. (Biopak, Merck, USA).

2.2. Synthesis of g-C_3N_4/WO_3 heterostructured nanocomposite

Silica-supported g-C3N_4/WO_3 was synthesized via a two-step heat treatment route. Initially, 20 g of urea was dissolved in 40 mL of deionized water (≥0.06 μS/cm). Afterward, 5 g of silica was added into the aqueous solution of urea to obtain a paste which was spread over a petri dish and left for drying overnight in an oven at 60 °C. The dried paste was further crushed in a mortar to a fine powder and annealed at 550 °C for 2 h in a muffle furnace in a self-supporting atmosphere to obtain silica-supported g-C_3N_4. After that, silica-supported g-C3N4 was sonicated in the solution prepared by dissolving tungstic acid in ammonia for 30 min and subsequently filtered. Finally, silica-supported g-C_3N_4 impregnated with ammonium paratungstate was annealed to 500 °C for 2 h to obtain silica-supported g-C_3N_4/WO_3.

2.3. Characterization methods

X-ray diffraction analysis was used to determine the crystalline phase structure of the nanocomposite using XRD diffractometer MiniFlex600 (Japan, RIGAKU) with Co cathode. The morphology of the samples was obtained by using NovaNanoSEM 450 scanning electron microscope (The Netherlands, FEI Company) and JEM-2100 transmission electron microscope (Jeol Ltd., Japan). The optical bandgap was evaluated using Lambda 1050 (PerkinElmer Inc., USA) spectrophotometer in diffuse reflectance mode. The specific surface area and pore size distribution were obtained from the adsorption/desorption of N_2 isotherms using Belsorp-mini, Japan. Identification of degraded by-products was performed on a quadrupole time of flight mass spectrometer (6530 Q-TOF, Agilent Technologies, Santa Clara, USA) employing an electrospray ion (ESI) source set to negative mode. Mass spectra were acquired over the m/z 100-1500 range at a scan rate of 3 scans·s^{-1}. Accurate mass measurements were obtained via a calibrating solution involving the use of internal reference masses TFA anion [$C_2O_2F_3(NH_4)$] at m/z 112.985587, and HP-0921 [hexakis-(1H,1H,3H-tetrafluoropentoxy)-phosphazene] ($C_{18}H_{18}O_6N_3P_3F_{24}$) at m/z 1033.988109). Data were recorded and processed in MassHunter software v.B.05.01 (Agilent Technologies).

2.4. Photocatalytic reaction setup and analysis

The photocatalytic activity of the as-prepared nanocomposite was evaluated by the elimination rate of $E1$ hormone under dark, UV, and visible light irradiation in a batch-wise mode. For each experimental run, a specific amount of photocatalyst powder was dispersed in a 12 mL aqueous solution of $E1$ hormone and irradiated for 3 h under a constant stirring rate of 450 rpm using a magnetic stirrer. The stock hormone solution was initially prepared at a concentration of 500 μg/L by adding 1 mg of $E1$ hormone into 2 L of HPLC-grade water, magnetically stirred at 800 rpm for 24 h, and stored under dark conditions. The prepared hormone solution was further diluted with HPLC-grade water to obtain different concentrations used throughout the study. Samples of concentrations 500, 400, 300, 200, and 100 μg/L were collected by a micropipette and into 2.5 mL HPLC vials using a 0.45 |rm glass microfiber filter. HPLC analysis was performed on samples in triplicates and resulting mean concentrations were plotted on the calibration curve. The photocatalytic degradation was carried out in a self-made enclosed wooden chamber in which GM electronics UV (~365 nm, OSV1YL5111A) and visible LEDs (~420 nm, 504UVC2E-Q6C) were mounted directly above the reaction beaker. LEDs were chosen instead of conventional lamps due to their narrow emission spectra and energy-cost benefits [**47**]. For evaluation of the antibacterial activity, the same setup was used in a sterilized fume hood.

2.5. High-performance liquid chromatography (HPLC) analysis

Standard calibration of $E1$ hormone was prepared according to the method previously devised by Yasir et al. on HPLC DionexUltiMate 3000 Series (Thermo Fisher Scientific, Germany), and the calibration curve was externally developed with Chromeleon version 7.2 software (Thermo Fisher Scientific, USA) with concentrations quantified accordingly [**48**].

2.6. Design and optimization of photocatalytic study

The photocatalytic process for the removal of the hormone was studied by the RSM using three selected numeric factors, i.e., hormone concentration (μg/L), photocatalyst dosage (μg), and solution pH, which were simultaneously investigated via Design-Expert 11.0v software. RSM is an excellent tool for establishing a relationship between several parameters and the response output of a system in the form of a second-order polynomial equation. A total of 17 experimental runs were randomly generated thereby allowing the study of linear, quadratic effects, pseudo-first-order, pseudo-second-order, and intra-particle diffusion kinetic models. The Box-Behnken design (BBD) polynomial quadratic model equation is presented below.

$$R = Y_0 + Y_1 A + Y_2 B + Y_3 C + Y_1 2AB + Y_1 3AC + \cdots \tag{1}$$

where R is the response (photodegradation), Y is the coefficient related to the factors, while A, B, and C represent the investigated factors in the model. This polynomial equation was further used for predicting the optimal removal parametric values using RSM experimental design based on the BBD model within low and high factor levels, as shown in **Table 1**.

Table 1 Investigated factors with their high and low levels within the experimental design space.

Factor	Name	Low level	High levels	Mean
A	Hormone conc. (μg/L)	100	500	300
B	Dosage (μg)	1000	5000	3000
C	pH of solution	3	9	7

2.7. Adsorption-desorption and photodegradation reusability test study

To evaluate the viability of the photocatalyst under repeated cyclic use, seven simultaneous experimental cycles were performed to examine the effectiveness of the nanocomposite in dark and visible light irradiation. The conditions were set as follows: 12 mL of 300 μg/L of $E1$, 3000 μg photocatalyst dosage, and 3 h of constant stirring at 450 rpm. After the experimental run, the solution was left for 30 min to let nanoparticles settle down and the sample was drawn carefully so that no powder was drawn into the filter during the aliquot extraction from the solution. Additionally, a reference sample value was recorded as the initial control solution concentration to calculate the removal efficiency for adsorption and photodegradation for each cycle. The solution containing the beaker was left to dry before the fresh hormone solution was poured from the stock solution for the next reusability cycle.

2.8. Statistical analysis

OriginLab 9.0v and Design expert software 11.0v were used for the statistical analysis and plotting of relevant graphs used throughout the study. For the determination of the significance of each experimental factor, single-factor ANOVA analysis was employed in which $p < 0.05$ was taken to be statistically significant. Determination of coefficient (R^2) was used to predict the suitability of the predicted model in comparison to the actual experimental data. Additionally, the sum of squared errors (SSE) and Chi-squared (x^2) values were calculated to minimize deviations from the response values.

2.9. Antibacterial activity testing

The bactericidal activities of the as-prepared silica-supported g-C_3N_4/WO_3 were evaluated against Escherichia coli and Staphylococcus aureus bacteria using the common agar plate method [**49**]. Firstly, a culture of bacteria was inoculated and incubated in a shaker overnight at 37 °C. By performing serial dilutions, the initial concentration of the bacterial inoculum was maintained at 6.0 x 106 CFU/mL. In a typical experiment, 10 mg of as-prepared nanocomposite was added to a 3 mL buffer solution in a beaker and stirred continually for 10 min prior to light irradiation. Aliquots of the irradiated solutions under UV, visible, and dark test conditions were taken after 1 h intervals and cultured in agar plates to form viable bacterial colonies. The concentrations of the remaining bacterial colonies were counted in triplicates and mean data were recorded. Images were also taken of the agar plates to visually depict the proliferation of the bacterial colonies.

3. Results and discussion

3.1. Morphological analysis

The as-prepared nanocomposite was morphologically characterized by the SEM and TEM as shown in **Fig. 1**. As can be seen, the nanocomposite exhibits coarse and rough morphology with a random distribution of WO_3 particles (bright spots) lodged inside the porous g-C_3N_4 mesh (**Fig. 1**a). While in the TEM image (**Fig. 1**b) it can be seen that the as-prepared nanocomposite is comprised of agglomerates of porous silica mesh and g-C_3N_4 in accordance with the SEM results. The morphology appears to be rough throughout the structure with the accumulation of large agglomerates having a consistent appearance throughout. Based on the TEM and SEM analysis, it can be inferred that a successful heterojunction of WO_3 and g-C_3N_4 was formed in a porous silica mesh. Moreover, EDX analysis was carried out to determine the amount of each elemental component at the selected bright region. From **Fig. 1**c, it can be observed that silica was present in the highest concentration along with oxygen while only 1.5 atomic % was detected for tungsten. No other impurities or other phase elements were detected.

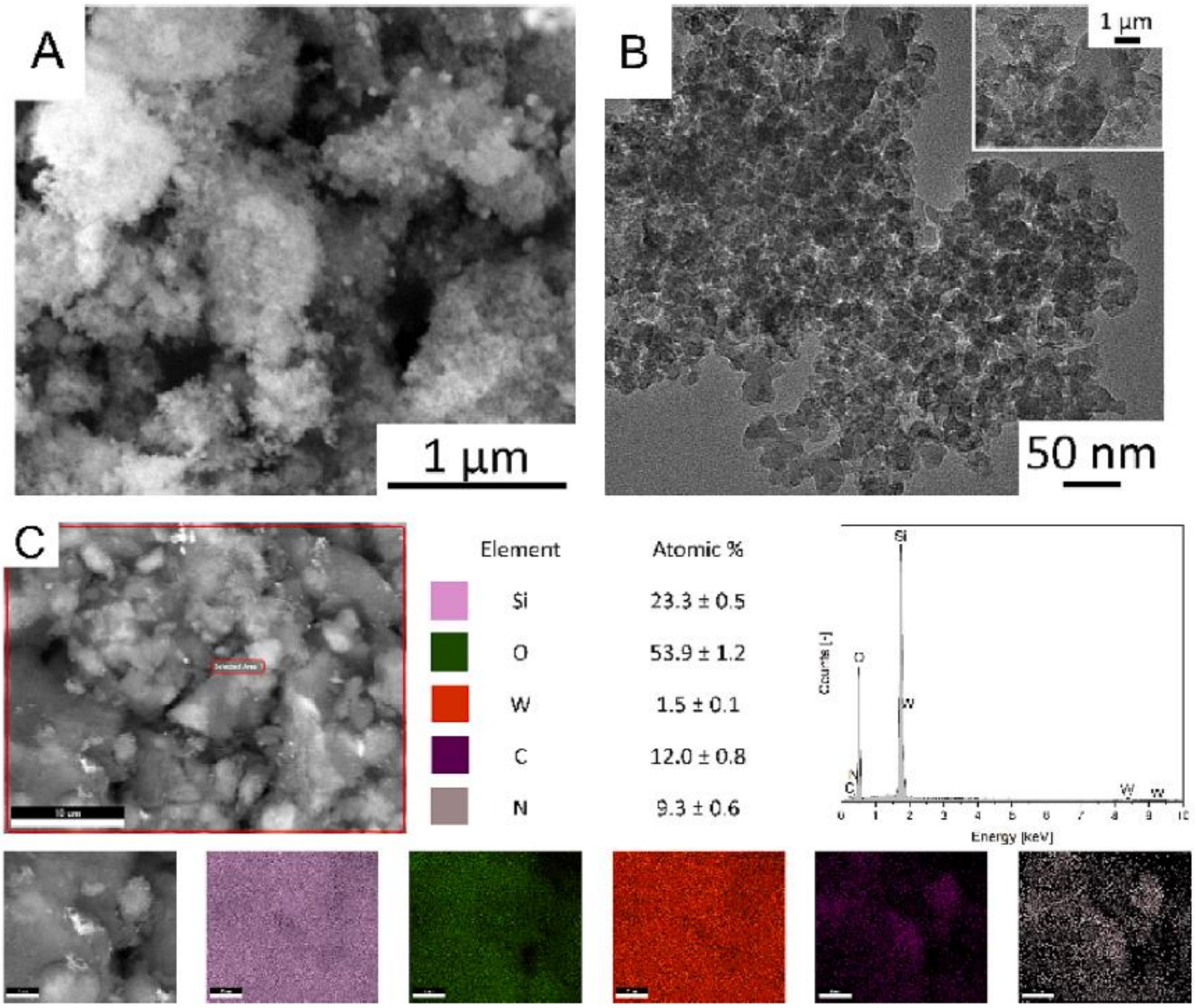

	Element	Atomic %
🟪	Si	23.3 ± 0.5
🟩	O	53.9 ± 1.2
🟥	W	1.5 ± 0.1
🟪	C	12.0 ± 0.8
🟫	N	9.3 ± 0.6

Fig. 1. SEM (a), TEM (b), and EDX analysis (c) of the as-prepared nanocomposite.

3.2. Structural analysis

Fig. 2a shows the XRD pattern of the as-prepared nanocomposite, i. e., the constructed assembly of $SiO_2 > g\text{-}C_3N_4 > WO_3$, in descending weight order. The XRD pattern for silica appears to be broad and of low intensity with a prominent peak at an angle of $2\theta = 23°$ confirming coarse grain size and with low crystallinity [**50,51**]. In the case of silica-supported g-C_3N_4, the XRD pattern reveals the presence of the most pronounced peak associated with the interplanar stacking of g-C_3N_4 appeared at 28.74°, corresponding to the (101) crystalline plane. While the other diffraction peak usually observed for g-C_3N_4 at an angle of 10.3° corresponding to (100) crystalline plane as reported in the literature was not so prominent, possibly due to highly dispersed silica particles on the surface of g-C_3N_4 [**52**]. Overall, in comparison to XRD patterns available in the literature for g-C_3N_4, less sharp peaks intensity was observed, an indication that a successful dispersion of silica particles as a support material was achieved. No other diffraction phases of impurities were detected. All intensity peaks can be indexed with the corresponding peaks reported in PDF Card No. 01-087-1522. For all samples, the inclusion of silica led to a pronounced effect on peaks intensitz and width, in accordance with the literature report [**53**]. It should be noted that evaluated XRD patterns have a slight shift in 20 of the peaks as compared to other literature reports due to the Cobalt-K alpha detector utilized in the study. For the silica-supported WO_3, the most prominent peaks observed at diffraction angles of 20 26.96°, 27.53°, and 28.34° can be ascribed to the (002), (020), and (200) planes of WO_3 (PDF Card No. 01-071-0305). In the case of the nanocomposite, all prominent peaks observed separately for WO3 and g-C_3N_4 appeared indicating a successful construction of a heterojunction. Additionally, $FT-IR$ analysis (**Fig. 2**b) was also carried out which revealed the presence of all typical peaks associated with the g-C_3N_4. Specifically, the peaks observed at 810 cm^{-1} and in the absorption region of 1600-1200 cm^{-1} were associated with the vibration of heptazine-derived units and stretching of C-N heterocyclic bonds, respectively, as per the available literature reports [**54,55**]. The peak at 802 cm^{-1} is assigned to the stretching of W-O-W bonds [**56**]. Moreover, all silica-supported samples exhibit characteristic silica peaks at 1084 cm^{-1} and 812 cm^{-1} attributed to the Si-O-Si bond stretching and Si-O symmetric bond vibrations, in accordance with a similar report [**57**]. The results indicate that the structural integrity of the g-C_3N_4 and WO_3 was maintained during the synthesis of the as-prepared nanocomposite.

3.3. UV-vis analysis

The optical bandgap and the electronic structure of a photocatalyst are important characteristic features that determine the potential of achieving an optimal rate of photoactivity. The optical band gap of the as-prepared sample can be calculated using the Tauc relation as follows [**58**]:

$$[\alpha h\nu]^{p} = A\left(h\nu - E_{g}\right) \tag{2}$$

where α is the optical absorption coefficient, hv stands for the energy of a photon with frequency v, A is the proportionality constant, E_g is the optical bandgap, and p represents the constant whose value is determined by the type of energy band transition.

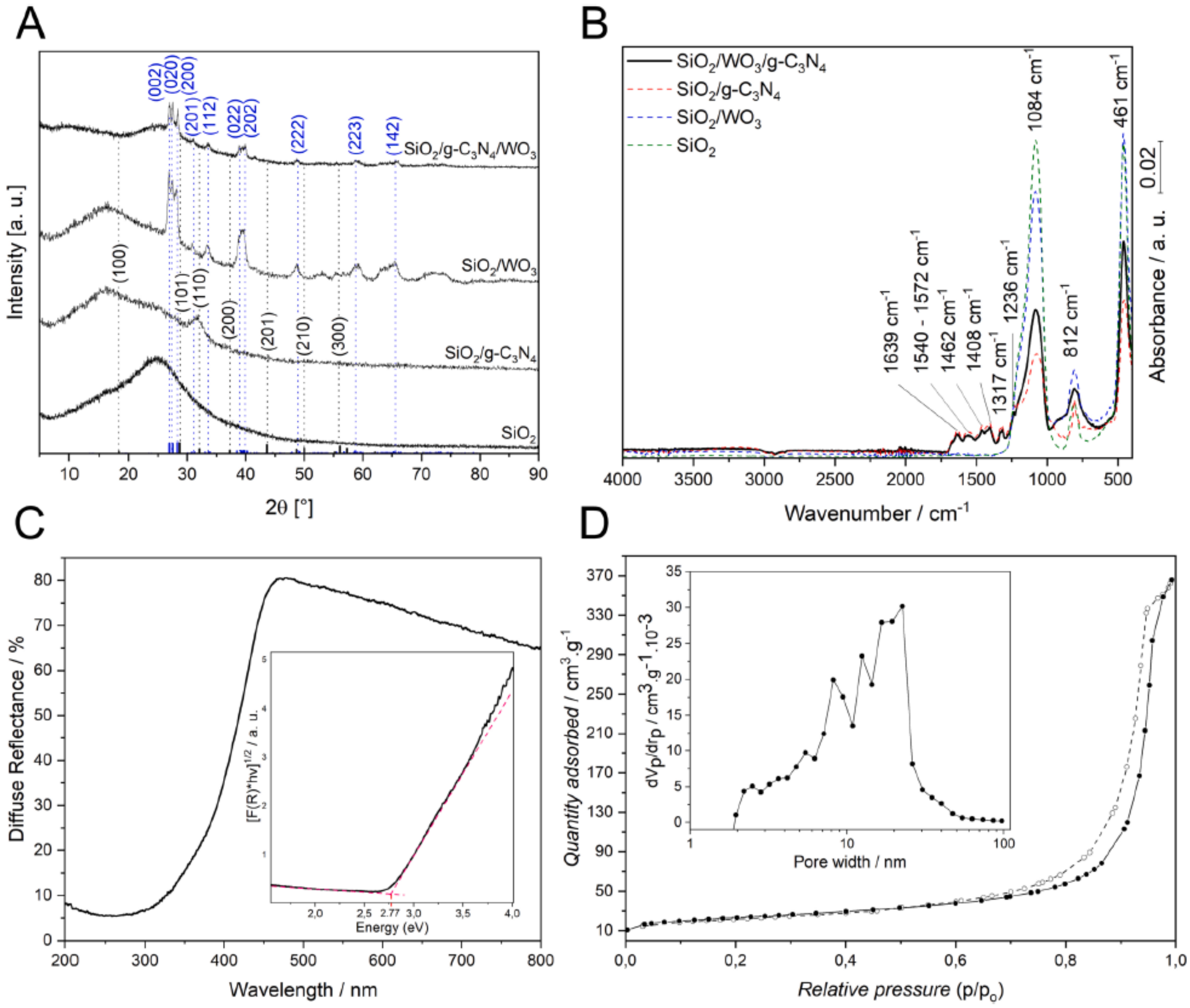

Fig. 2. XRD (a), $FTIR$ (b), UV-vis DRS and K-M function in inset (c), and (d) BET surface area and pore size distribution (inset) of the as-prepared nanocomposite.

Since UV-vis diffuse reflectance data was obtained (**Fig. 2**c), Kubelka-Munk function which correlates the reflectance spectra with the absorbance coefficient in eqn. (2) was applied as follows:

$$F(R) = \frac{\alpha}{s} = \frac{(1-R)^2}{2R} \tag{3}$$

where $F(R)$ is Kubelka-Munk function, R is reflectance, and s is the scattering factor which is wavelength independent. As $F(R)$ is proportional to a, the exponential value can be obtained by plotting a graph between $[F(R) - h\nu]^p$ and hv. The best fit to the straight line near the absorption edge was found for $1/2$ indicating an indirect allowed transition for the nanocomposite. Finally, the optical bandgap value of the sample was obtained by plotting a graph between $[F(R) - h\nu]\frac{1}{2}$ and photon energy ($h\nu$) and extrapolating the graph slope to $[F(R) - h\nu]\frac{1}{2}$ = 0 as shown in **Fig. 2**c (inset). The optical bandgap value for the nanocomposite was estimated to be 2.70 eV. The obtained bandgap value is in accordance with the commonly reported bandgap values for the g-C_3N_4/WO_3 hybrid photocatalysts in the literature.

3.4. BET surface area analysis

The BET surface area of photocatalytic semiconductors plays a crucial role in determining the photoactivity by providing exposed crystal facets where the photocatalytic reaction proceeds as well as providing abundant adsorptive sites. The BET surface area and pore size distribution of the silica-dispersed g-$C3N_4$/WO_3 were investigated by the nitrogen adsorption-desorption as shown in **Fig. 2**d. As can be seen, the obtained isotherm exhibits a close resemblance to the type V isotherm, an indication of the mesoporous and microporous structure of the nanocomposite, according to the IUPAC classification [**59**]. While the H1 hysteresis loop of isotherm indicates the existence of relatively high pore size uniformity and pore connectivity. The H1 loop is commonly reported for mesoporous silica templated materials and carbon-based materials, as such in the case of the synthesized nanocomposite [**60**]. The pore volume distribution (**Fig. 2**d inset) reveals the nonuniform distribution of the nanocomposite, mainly due to the contribution from the highly porous structure favored by the presence of silica and polymeric g-C_3N_4. The BET surface area of the nanocomposite was calculated as 83.3 m^2/g, which is higher than similar reported g-C_3N_4-based nanocomposites [**26**]. The higher surface area could prove beneficial to achieve an effective rate of photocatalytic degradation of $E1$ hormone.

3.5. Preliminary evaluation of photocatalytic degradation

For the response surface optimization, a preliminary evaluation of the photoactivity was carried out by varying the concentration of the hormone in the range of 100 to 500 μg/L. This range was selected based on the results of our previous experiments reported in the literature and taking into account given solubility of $E1$ hormone in water which forms a maximum plateau at 600 μg/L over a study period of one month, as reported [61]. Other operational conditions were set as follows: photocatalyst dosage of 3000 μg in a beaker containing 12 mL of hormone solution at pH 7, stirred at 450 rpm for 3 h. As can be seen from **Fig. 3**, a total photocatalytic degradation was achieved with the selected parameters up to 300 μg/L hormone concentration, whereas a slight decrease was observed under visible light irradiation when using 400 and 500 μg/L of solution concentration. Interestingly, the adsorption of $E1$ on the photocatalyst decreased (ranging from 17.1 to 1.1%) with increasing hormone concentration (100 to 500 μg/L) which is expected because the surface area of photocatalyst is nearly constant for each experimental run while a higher concentration of $E1$ allows only a fixed number of adsorption sites to be filled to reach saturation. Based on the obtained data, analysis by the BBD model was carried out using three factors, with each having low, medium, and high levels.

3.6. Optimization by response surface methodology

The optimized experimental parameters for the photocatalytic degradation system were obtained by analyzing the experimental data using a three-level experimental matrix generated by the BBD model together with experimentally obtained responses, as shown in **Table 2**. A total of 17 experimental runs were performed in a random order to avoid any systematic bias while other non-dominant process factors not selected for the study were treated as an error. Based on the obtained results, three empirical relationships (eqn. (**4**), 5, and 6) generated are presented below. These equations describe the photocatalytic removal efficiency in terms of three selected parameters and their coefficients corresponding to the linear and quadratic components. The three independent variable factors investigated in the optimization study include the initial concentration of the hormone, photocatalyst dosage, and solution pH, labeled as A, B, and C, respectively. The positive and negative signs indicate whether terms have synergistic or antagonistic effects on the response variable.

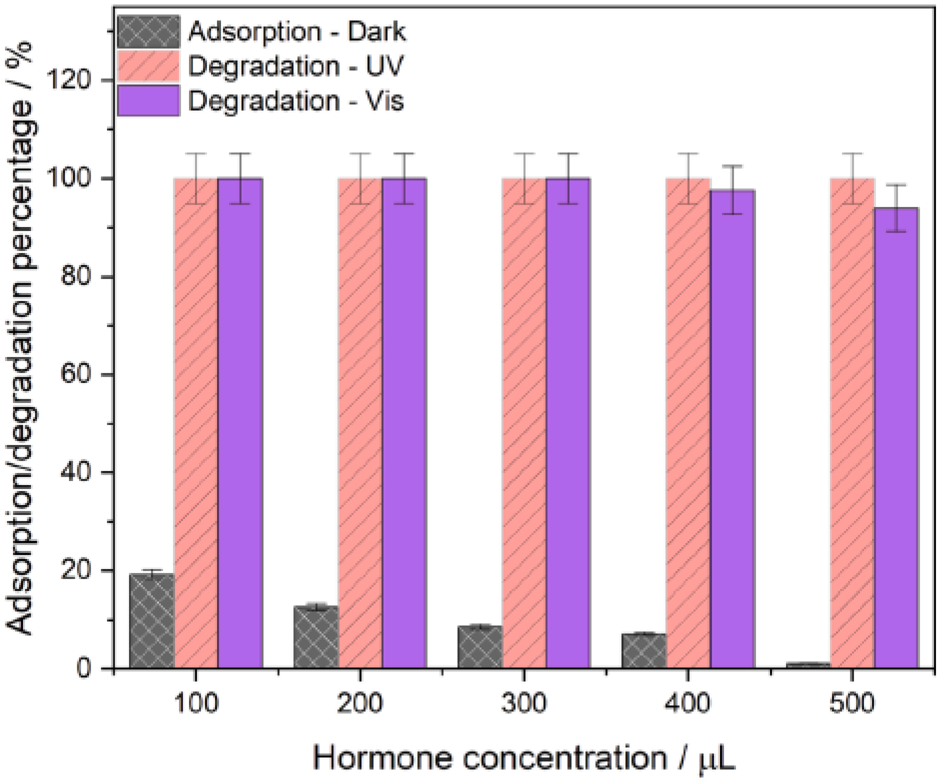

Fig. 3. Preliminary results of adsorption and photocatalytic degradation of $E1$ hormone at varying concentrations (100-500 μg/L) under UV and visible light irradiation.

For a visual representation, the predicted and actual experimental responses were plotted in Fig. 4a. The plotted graphs reveal that both predicted and actual values lie in close vicinity of each other and in accordance with the degree of coefficient of determination for the UV and visible light irradiation. Moreover, no ambiguous data points were observed in the externally studentized residuals graphs (**Fig. 4**b).

$$\begin{aligned} \mathit{Removal\%} - \mathit{Dark} = {} & +23.00 - 0.38A + 2.07B - 1.05AB - 5.08AC \\ & - 1.69BC - 7.08A^2 - 7.22B^2 - 1.68C^2 \end{aligned} \tag{4}$$

$$\begin{aligned} \mathit{Removal\%} - \mathit{UV} = {} & +99.75 - 3.19A + 3.63B + 1.88C + 2.13AB \\ & + 3.12AC - 2.91BC + 0.51A^2 - 2.64B^2 - 3.39C^2 \end{aligned} \tag{5}$$

$$\begin{aligned} \mathit{Removal\%} - \mathit{Vis} = {} & +95.62 - 4.21A + 6.45B + 5.16C + 2.47AB \\ & + 4.28AC - 5.92BC - 3.08A^2 + 1.40B^2 - 10.27C^2 \end{aligned} \tag{6}$$

3.7. Analysis of variance study (ANOVA)

$ANOVA$ study was performed on the developed model to determine the significance of the main influencing factors on the response rate of the photocatalytic process and the results are presented in **Table 3**. Specifically, Fisher value (F-value) and p-values were used to verify the significance of each coefficient of the developed mathematical model.

The model F-values were calculated as 2.07, 18.03, and 11.01 under dark, UV and visible light irradiation, respectively. This implies the model is not significant for the removal of E1 hormone in dark and there is a 17.54% chance that an F-value this large could occur due to noise. However, the model was observed to be significant for UV and visible conditions indicating there is a $<$0.30% chance that F-values this large could occur due to noise. P-values for the different investigated terms were also evaluated. P-values less than 0.05 indicate the model terms are significant. In this case, A^2 and B^2 model terms demonstrated to be significant removal of the hormone in dark conditions. While A, B, C, AB, AC, BC, B^2, and C^2 were observed to be significant model terms for hormone degradation under UV. For the hormone degradation in the visible light range, A, B, C, AC, BC, and C2 were observed to be significant model terms. Comparing the experimental value R^2 to the predicted R^2 value a large difference between the values for the removal of the hormone in dark light conditions was observed while a close agreement with a difference of less than 0.2 was observed for the UV and visible light degradation process. Furthermore, adequate precision values were also measured representing a low signal-to-noise ratio. A ratio greater than 4 is desirable. According to the results, ratios of 3.88, 14.22, and 10.82 were obtained for the adequate precision signals for the removal of the hormone in dark, UV, and visible light conditions, respectively. This showed that the model could be used to navigate the design space for UV and visible light degradation processes as opposed to the dark conditions.

3.8. Two-factor interaction effects on the removal of hormone

The $3D$ response surface graphs were plotted to thoroughly evaluate the influence of experimental variables on the response. The observations obtained from two-factor interaction parameters on the response are discussed below:

Fig. 6a shows the effect of photocatalyst dosage and initial concentration of $E1$ on the adsorption removal percentage of $E1$. As can be seen, the removal efficiency gradually increases with increasing dosage at a constant hormone concentration due to the presence of a large surface area available at high dosage, with greater availability of sites for adsorption [**62**]. Whereas, at a constant dosage, the removal efficiency increases with an increase in hormone concentration up to 300 μg/L, and then a slight decrease is observed when the solution is in excess. The optimum hormone concentration is seen at 300 μg/L and dosage of 3000-5000 μg at which the removal efficiency is nearly 20% compared to 500 μg/L hormone concentration and 1000 μg dosage where it is reported to be below 10%. The low removal percentages are reported owing to the low amount of the powdered sample present for interaction with $E1$.

Table 2 The experimental runs with their actual and predicted responses.

Runs	Factors			Responses					
				Adsorption-Dark		Degradation-UV		Degradation-Vis	
	A	*B*	*C*	*Actual*	*Predicted*	*Actual*	*Predicted*	*Actual*	*Predicted*
	μg/L	μg		%	%	%	%	%	%
1	300	1000	9	9.20	11.49	92.90	94.87	88.40	91.38
2	100	5000	7	16.50	14.65	100.00	100.52	100.00	99.31
3	300	3000	7	23.20	23.20	100.00	100.00	96.20	96.20
4	100	3000	3	6.70	8.40	100.00	101.26	83.50	85.60
5	100	1000	7	14.60	7.29	100.00	99.44	100.00	95.31
6	500	3000	3	22.20	17.80	87.50	88.74	70.10	68.62
7	500	5000	7	1.10	8.41	100.00	100.56	94.00	98.69
8	300	3000	7	23.20	23.20	100.00	100.00	96.20	96.20
9	300	1000	3	9.40	12.57	86.20	85.31	68.20	69.22
10	500	3000	9	14.70	9.94	100.00	98.72	91.40	87.50
11	300	3000	7	23.20	23.20	100.00	100.00	96.20	96.20
12	300	5000	9	24.00	19.01	95.80	96.33	94.80	92.44
13	300	5000	3	13.80	13.33	100.00	98.39	95.60	93.95
14	100	3000	9	13.40	20.86	100.00	98.78	84.10	87.37
15	300	3000	7	23.20	23.20	100.00	100.00	96.20	96.20
16	300	3000	7	23.20	23.20	100.00	100.00	96.20	96.20
17	500	1000	7	3.40	5.25	91.50	90.98	84.10	84.79

In **Fig. 6**b, the effect on $E1$ adsorption removal percentage is observed by varying solution pH and concentration of the hormone solution. The pH is varied from 3 to 9 and at 100 μg/L hormone concentration, the removal efficiency increases from 5% to slightly above 20%. At lower pH, efficiency is low which could be attributed to the competition between the hydronium ions (H^+) and the $E1$ hormone for the binding sites available on the adsorbent surface [**63**]. Similarly, at a constant pH, the removal efficiency improves from 100 to 300 μg/L and then a plateau is achieved up to 500 μg/L because an excess amount of $E1$ hormone is present in the solution. The optimum value of removal efficiency approximately 23% is obtained at 300 μg/L concentration, regardless of variation in solution pH. The pH of the reaction medium greatly affects the surface charge and tendency of ionization of the reactants in the photocatalytic system. To establish the role of pH on the elimination rate of $E1$ hormone, the pH at zero surface charge (pHPZC) was calculated for the as-prepared nanocomposite using the salt addition method at room temperature according to the procedure described by Bakatula et al [**64**]. The obtained pHPZC for the nanocomposite was evaluated to be 4.26 as shown in **Fig. 5**. This indicates that the as-prepared nanocomposite possesses a positive surface charge at pH < 4.26 and a negative charge at pH $>$ 4.26. The results in **Fig. 6**b, depict that the adsorption of $E1$ hormone by the nanocomposite was regardless of the effect of pH in the range of 3-9. This is because the acid dissociation constant (pKa) for $E1$ is 10.34 indicating that at pH $<$ 10.34, $E1$ hormone will remain undissociated as a neutral molecule [**65**]. Therefore, there will be no contribution of electrostatic charge attraction in adsorption between the $E1$ hormone and photocatalyst.

Fig. 6c depicts the effect of solution pH and dosage of photocatalyst on the adsorption removal percentage of $E1$. As can be seen, the effect of varying dosage on removal efficiency is achieved regardless of solution pH. At any particular dosage, the removal efficiency remains constant with the variation in pH. The lowest efficiencies are reported at the lowest dosage of 1000 μg of photocatalyst due to a limited number of adsorption sites for $E1$ hormones. The removal percentage is directly dependent on the dosage of the photocatalyst creating more numerous sites for adsorption interaction and reaching a maximum efficiency of around 23% [**65**]. However, at values above 3000 μg, a drop in removal percentage can be seen owing to the high remaining concentration of $E1$ hormone present in the solution, and the photocatalyst particles might agglomerate leading to low surface area for interaction with $E1$ hormones and hence obtaining lower removal output.

In **Fig. 6**d, the effect of changing the concentration of $E1$ hormone and dosage of photocatalyst is seen on the photodegradation removal percentage under UV light. The results are apparent that at high $E1$ concentrations, the effect of dosage is significant due to the sufficient amount of hormones present to interact with the photocatalyst surface. Hence, the value ranges from 85 to 100% when the dosage is increased from 1000 to 5000 μg. At low $E1$ concentrations, removal percentages are high, and a very minor improvement is observed by increasing the dosage. The removal percentage is nearly 98% at 1000 μg of dosage and 100 μg/L of $E1$ concentration and saturation is achieved by increasing the dosage to 3000 μg because of the negligible amount of E1 hormones left in the solution to be degraded by the photocatalyst [**62**]. Therefore, enhancing the dosage at this value is useful only at higher concentrations of $E1$.

Fig. 6e illustrates the effect of the initial concentration of $E1$ hormone and solution pH on the photodegradation removal percentage of $E1$ under UV light. The figure depicts a similar behavior of an increase in solution pH from 3 to 9 or a decrease in the concentration of $E1$ hormone resulting in an increase in the removal percentage [**65**]. At a constant $E1$ concentration of 500 μg/L, the removal percentage rises from 85% at pH 3 to approximately 98% at pH 7-9. On the other hand, at any specific pH, the efficiency increases at constant dosage with the decrease in E1 initial concentration because, at lower concentrations, photodegradation by a sufficient amount of heterostructured photocatalyst is higher due to being high surface area causing more interaction to be the dominant factor [**62**]. Generally, the removal percentage is lower at acidic pH conditions ranging from 85 to 100% whereas, at pH above 6, the minimum removal percentage is nearly 95% or higher. Thus, at neutral pH, the concentrations of $E1$ hormone ranging between 100 and 300 μg/L are suitable for the complete removal of $E1$ hormones from the water solution.

Fig. 6f shows the influence of the solution pH and the dosage of the photocatalyst on $E1$ photodegradation removal percentage under UV light irradiation. As can be seen, the pH has the more dominant effect on removal percentage at lower values of dosage. A linear rise in removal percentage was seen with an increase in pH because $E1$ remains undissociated in this pH range till pH reaches its value of pKa (10.34) [**65**]. For example, at a dosage of 1000 μg, the removal percentage is raised from below 85% to about 95% by varying pH from 3 to 9. Also, at lower pH of 3, the removal percentage is increased from above 80% to approximately 98% by increasing the dosage from 1000 to 5000 μg. The highest removal percentage is experienced at higher pH (5-8) and higher values of dosage 3000-5000 μg.

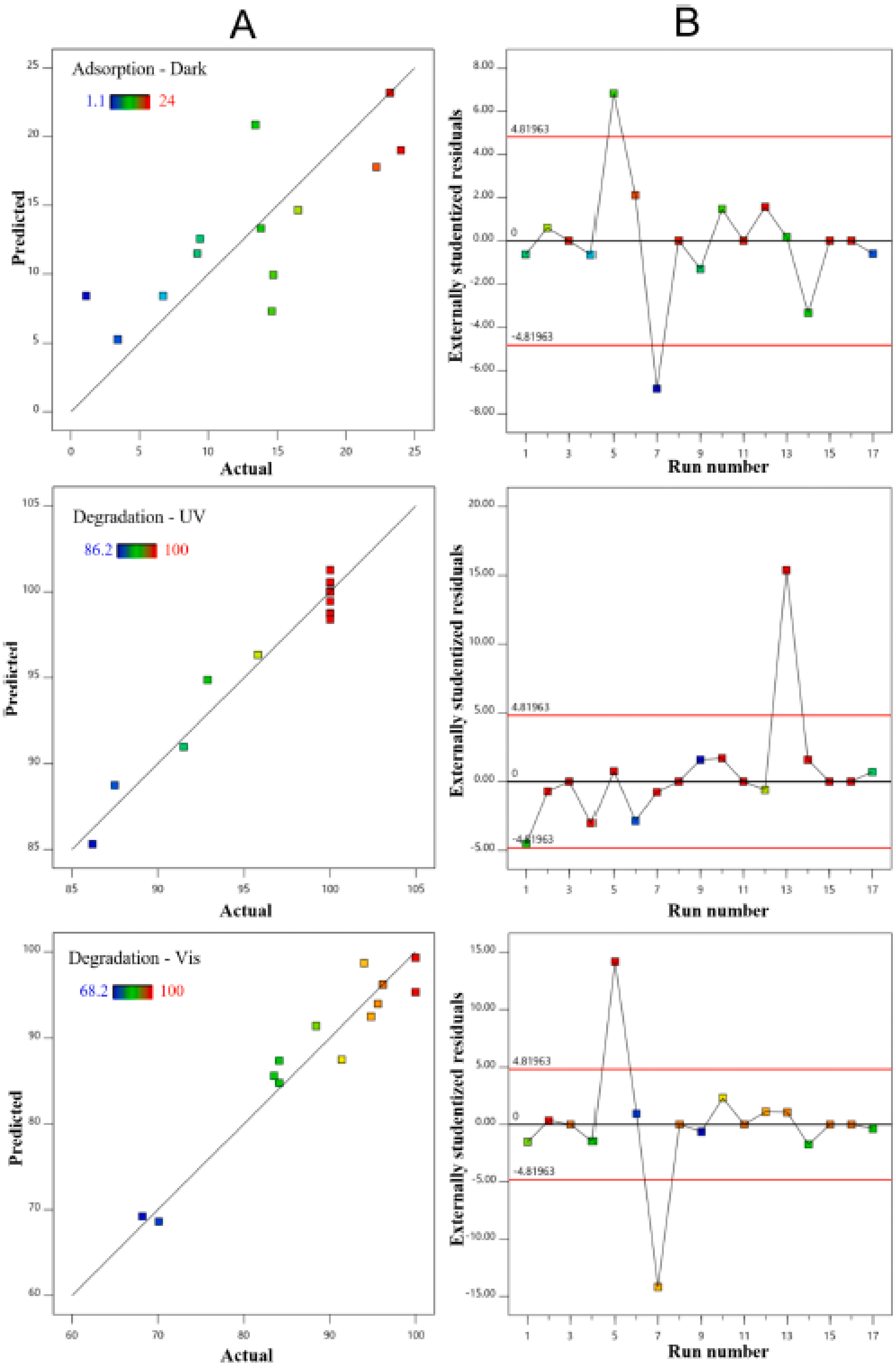

Fig. 4. Response plots of predicted vs actual experimental results (a) and externally studentized residuals (b) for $E1$ hormone removal under dark, UV, and visible light conditions.

Table 3 $ANOVA$ values for removal of $E1$ hormone based on BBD quadratic model design.

Source	Adsorption-Dark		Degradation-UV		Degradation-Vis		
	F-value	*p*-value	*F*-value	*p*-value	*F*-value	*p*-value	
Model	2.07	0.1754	18.03	0.0005	11.01	0.0023	Significant
A-Hormone conc.	0.03	0.8674	35.14	0.0006	9.88	0.0163	
B-Dosage	0.89	0.3759	46.93	0.0002	23.14	0.0019	
C-pH of solution	0.29	0.6064	13.15	0.0084	15.61	0.0055	
AB	0.12	0.7379	8.44	0.0228	1.79	0.2223	
AC	2.99	0.1274	19.20	0.0032	5.66	0.0490	
BC	0.33	0.5829	16.66	0.0047	10.82	0.0133	
A^2	5.79	0.0470	0.517	0.4954	2.91	0.1315	
B^2	6.04	0.0436	13.69	0.0077	0.60	0.4625	
C^2	0.24	0.6369	16.88	0.0045	24.27	0.0017	
Lack of Fit	254.64		14.97		95.62		Not significant
R^2	0.726		0.958		0.934		
Predicted R^2	0.375		0.905		0.849		
Adeq Precision	3.88		14.22		10.82		
Mean	15.59		97.29		90.31		
Std. Dev.	38.69		1.46		3.70		

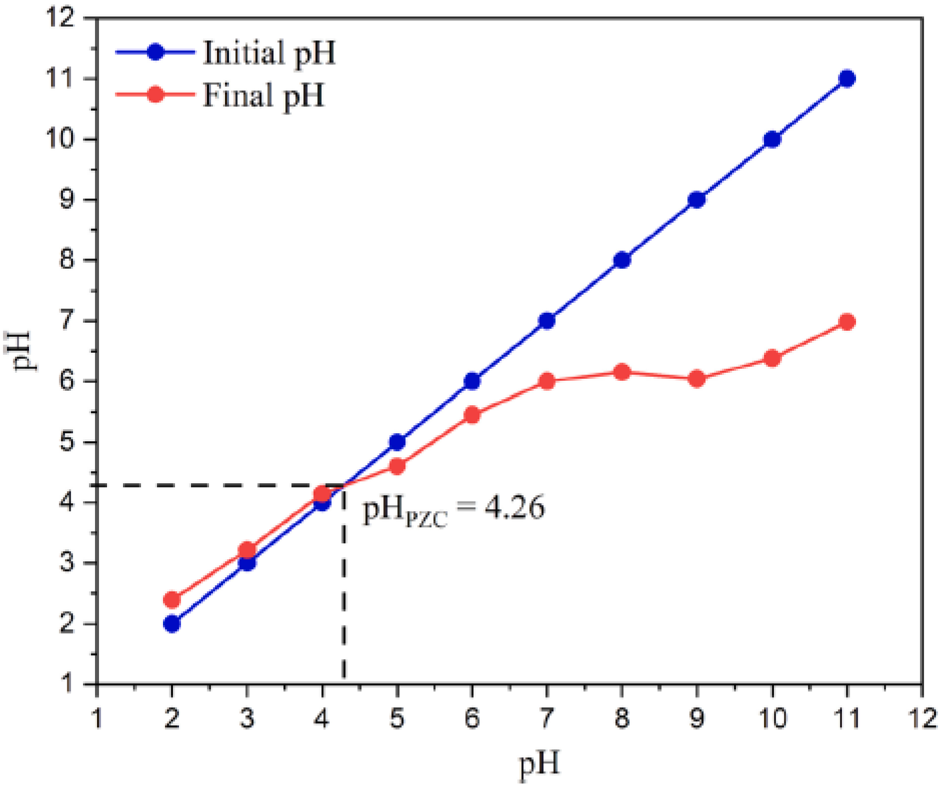

Fig. 5. Point of zero charge (pHPZC) of the as-prepared nanocomposite determined by salt addition method.

In **Fig. 6**g, the effect of changing the concentration of $E1$ hormone and dosage of photocatalyst is seen on the photodegradation removal percentage using visible light. The results indicate that the highest removal percentage is achieved at 5000 μg of dosage and $E1$ concentrations below 400 μg/L. Whereas, the least removal percentage is observed at 1000 μg of dosage of photocatalyst with 500 μg/L concentration of $E1$ hormone. The plausible reason could be that less photodegradation activity is achieved with the least dosage leading to less surface area for interaction and at higher concentrations of $E1$ hormone, the dosage is insufficient to degrade the whole solution completely [**62,63**].

Fig. 6h illustrates the effect of the initial concentration of $E1$ hormone and solution pH on the photodegradation removal percentage of $E1$ using visible light. As can be seen, the least removal percentage is observed at low pH of 3 and the highest concentration of 500 μg/L of $E1$. The removal percentage gradually increases ranging from 60 to 82% as $E1$ concentration is decreased from 500 to 100 μg/L at constant pH of 3. Similarly, when the concentration is kept fixed at 500 μg/L, there is a rise in the removal percentage from 60 to 88% because the competition between the hydronium ions (H+) and the $E1$ hormone for the binding sites is decreased by increasing the pH [**63**]. However, solution pH has the least effect on removal efficiency at low concentrations of $E1$ hormone because the photodegradation activity remains above 82% owing to the significant dominance of photocatalyst amount and reaches a maximum value of around 97% at neutral pH of 7.

Fig. 6i represents the influence of the solution pH and the dosage of the photocatalyst on $E1$ photodegradation removal percentage under visible light irradiation. As can be seen, the removal percentage increases linearly with the increase in dosage of the photocatalyst ranging from 1000 to 5000 μg at low pH values from 3 to 5 due to more surface area present by increasing dosage for interaction between $E1$ and photocatalyst [**62**]. The efficiency improves from 60% at 1000 μg to above 90% at 5000 μg of dosage. However, at higher pH $>$ 6, the removal efficiency remains high above 85%, and dosage did not have a significant effect in improving the efficiency. The highest efficiency of almost complete removal of $E1$ hormones (within the limit of detection) is reported at pH 7 with a dosage of 3000 μg and above.

3.9. Optimization validation

To confirm the validity and accuracy of the developed mathematical model, additional experiments were performed with the optimized parameters obtained by the RSM and compared with the actual experimental values as compared with the actual values as shown in Table 4. The values observed were 26.52%, 95.69%, and 92.40% for the adsorption, UV, and visible light irradiation, respectively, which were in close approximation to the predicted values (23.2%, 100%, and 96.2%) with a low degree of standard deviation. These results further confirmed the validity of the as-prepared nanocomposite mathematical model to selectively target persistent bio toxicants.

3.10. Effect of contact time and kinetic model study

The gradual increase in the adsorption/degradation capacity of $E1$ hormone with respect to time was carried out at different time intervals as shown in **Fig. 7**a. As can be seen, a rapid linear increase in the degradation capacity is observed for both UV and visible light irradiation, reaching a plateau after 90 min. Subsequently, a very slow degradation is observed for an additional 90 min, indicating a saturation rate was already attained. However, in the case of adsorption under dark conditions, a slower rate is initially observed till 60 min, which gradually increased till the observed duration of 180 min. For the present study, the kinetics of the as-prepared nanocomposite were also investigated in detail at the optimized conditions to obtain the rate constant value for the photodegradation of $E1$ hormone. Generally, a selection of kinetics models best fitted for the process parameters assists in the determination of actual optimized removal rates [**66**].

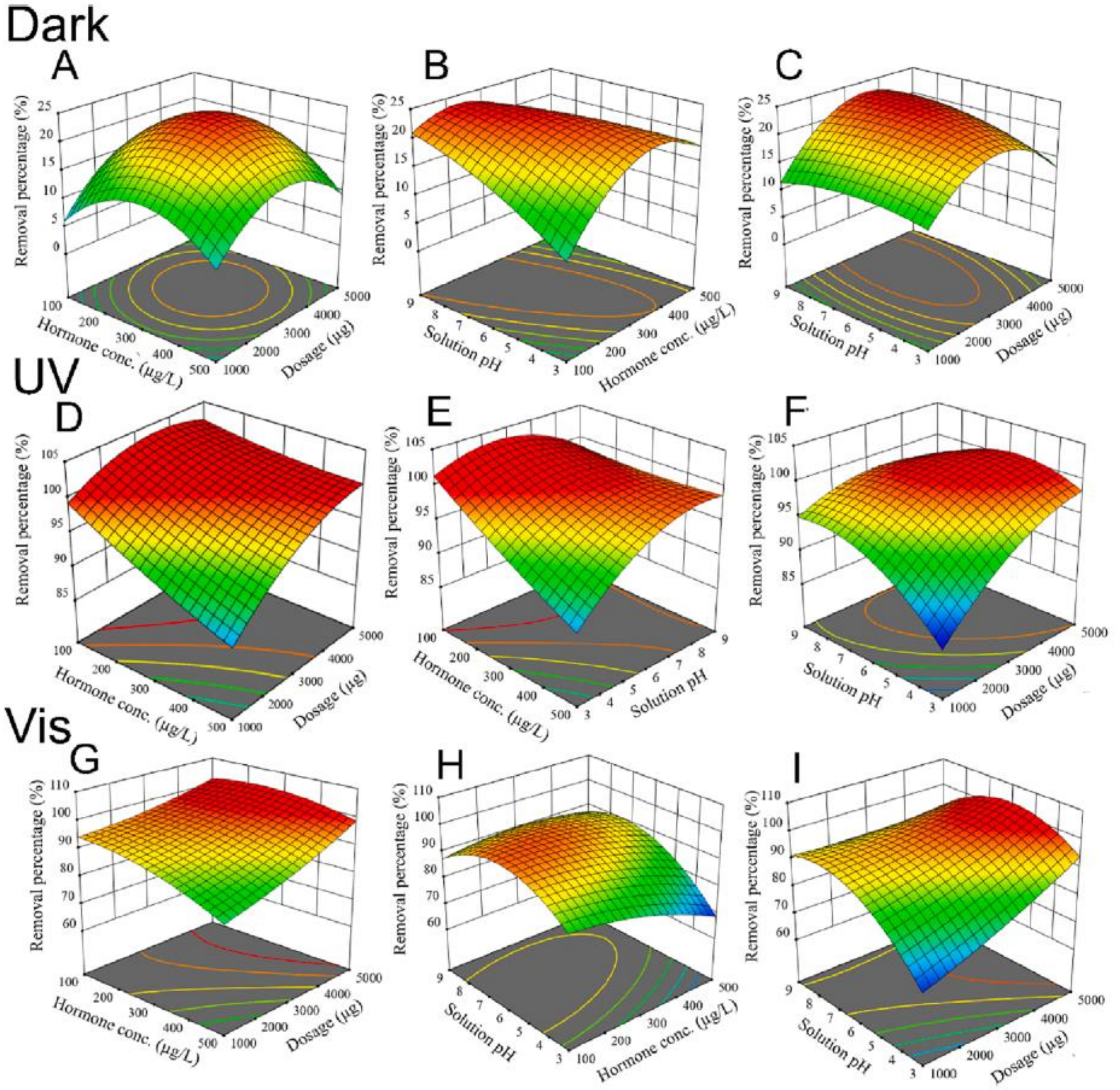

Fig. 6. 3D surface response plots of two-parameter interaction on the removal of $E1$ hormone under dark, UV, and visible light conditions.

Table 4 Point prediction and validation of optimized parameters (3000 μg of photocatalyst dosage, 300 μg/L of hormone concentration, and pH 7) at a 95% confidence interval.

Response	Predicted Mean	Observed	Std Dev	SE Mean	95% CI low for Mean	95% CI high for Mean	Desirability
Dark	23.2	26.52	6.03	2.69	16.82	29.57	1.00
UV	100	95.69	1.46	0.65	98.45	100.00	1.00
Vis	96.2	92.40	3.69	1.65	92.29	100.00	1.00

This is due to the fact that photodegradation is a function of several dominant and nondominant factors which contribute towards photodegradation, as such in a complex system. In this study, three commonly used kinetics models; pseudo-first-order, pseudo-second-order, and Weber-Morris intraparticle diffusion were investigated using the data generated from the experimental runs. The equations for these kinetics models are expressed as follows while the plotted graphs and values are given in **Fig. 7**b-d and **Table 5**, respectively.

$$\log(q_e - q_t) = logq_e - \frac{k_1}{2.303}t \tag{7}$$

$$\frac{t}{q_t} = \frac{1}{k_2 q_e^2} + \frac{t}{q_e} \tag{8}$$

$$q_t = k_3 t^{0.5} + C \tag{9}$$

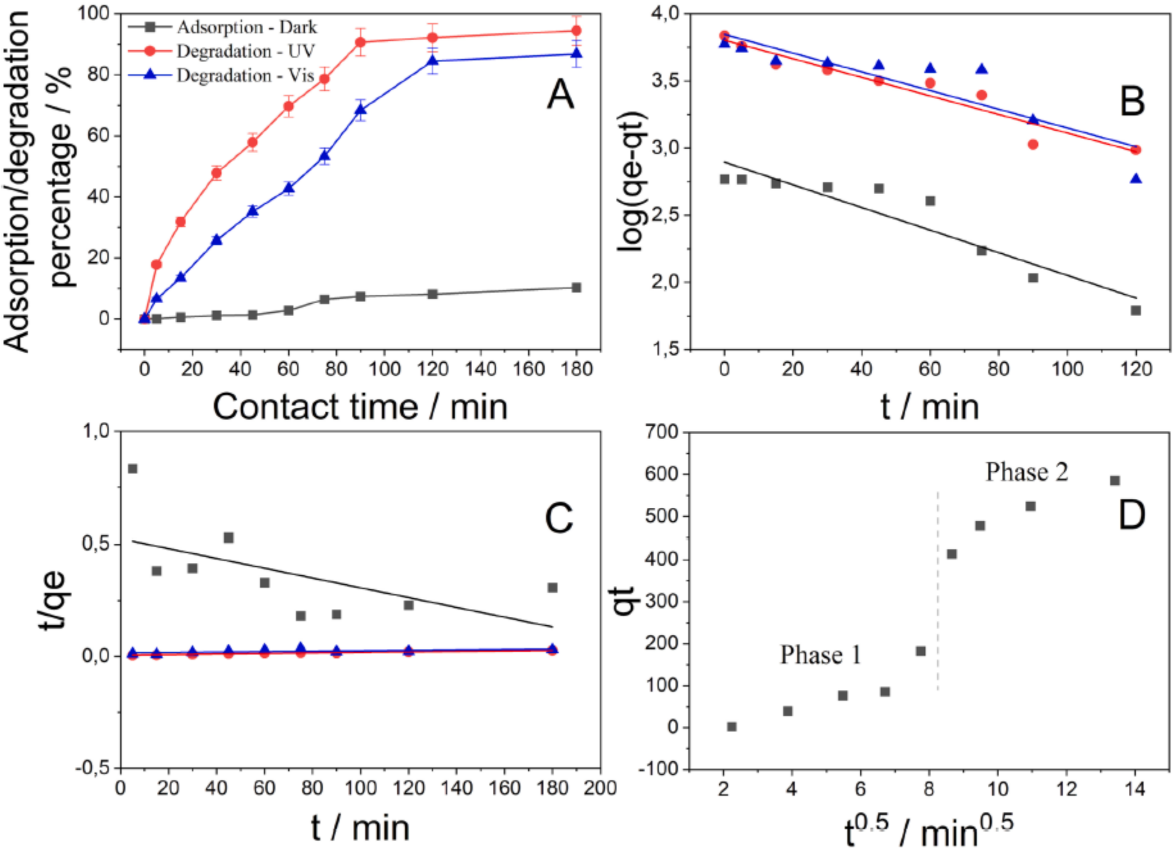

Fig. 7. Plots of the contact time (a), pseudo-first-order (b), pseudo-second-order (c), and intraparticle diffusion model (d) on the removal kinetics $E1$ hormone under dark, UV, and visible light conditions.

Table 5 Kinetic models and their determined parameters related to the removal of $E1$ hormone under dark, UV, and visible light conditions.

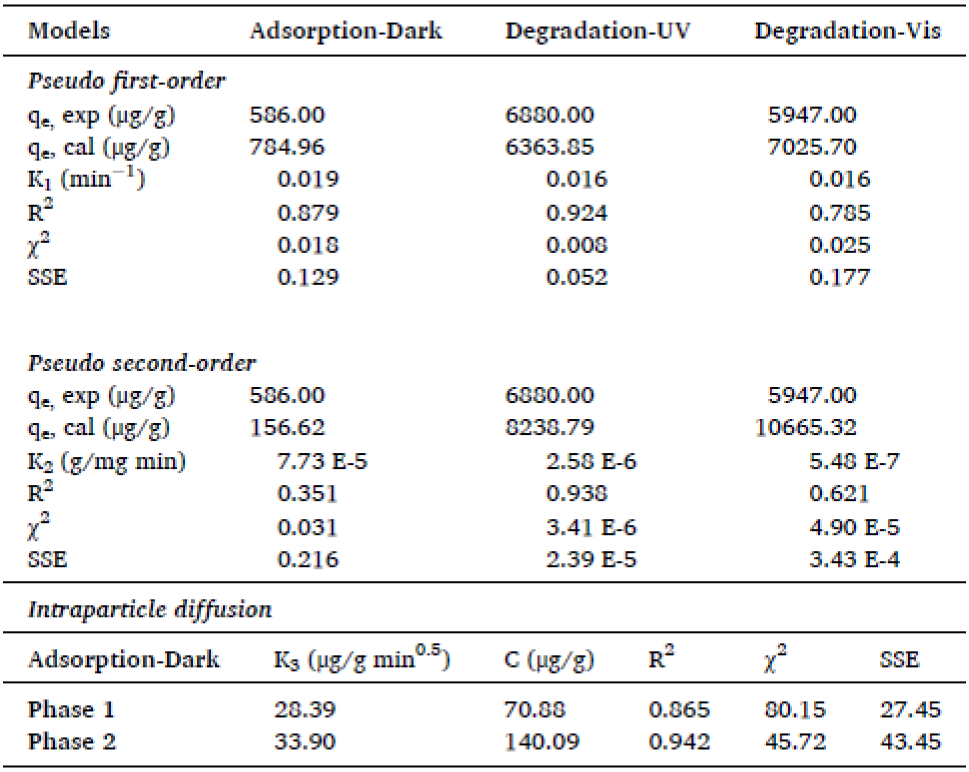

Models	Adsorption-Dark	Degradation-UV	Degradation-Vis
Pseudo first-order			
q_e, exp (μg/g)	586.00	6880.00	5947.00
q_e, cal (μg/g)	784.96	6363.85	7025.70
K_1 (min^{-1})	0.019	0.016	0.016
R^2	0.879	0.924	0.785
χ^2	0.018	0.008	0.025
SSE	0.129	0.052	0.177
Pseudo second-order			
q_e, exp (μg/g)	586.00	6880.00	5947.00
q_e, cal (μg/g)	156.62	8238.79	10665.32
K_2 (g/mg min)	7.73 E-5	2.58 E-6	5.48 E-7
R^2	0.351	0.938	0.621
χ^2	0.031	3.41 E-6	4.90 E-5
SSE	0.216	2.39 E-5	3.43 E-4

Intraparticle diffusion

Adsorption-Dark	K_3 (μg/g $min^{0.5}$)	C (μg/g)	R^2	χ^2	SSE
Phase 1	28.39	70.88	0.865	80.15	27.45
Phase 2	33.90	140.09	0.942	45.72	43.45

where q_e and q_t represent the removal capacity at equilibrium and time, t, respectively. The rate constants of pseudo-first-order and second-order values are denoted as k_1 and k_2, respectively. For the Weber-Morris equation, k_3 represents the intraparticle diffusion rate constant, and C is constant representing the boundary layer effect which influences the rate-limiting adsorption step.

Comparing **Fig. 7**b and 7c, it can be seen that the experimental capacities 586.0, 6880.0, and 5947.0 μg/g strongly follow the calculated capacities of the pseudo-first-order (784.96, 6363.9, and 7025.7 μg/g) for adsorption, UV and visible light irradiation, respectively, compared to the calculated values of pseudo-second-order (156.6, 8238.8, and 10665.3 μg/g), as shown in **Table 5**. This implies that a better fit is obtained for the first-order kinetics. Thus, the adsorption and photocatalytic hormone removal of $E1$ under UV and visible light of the as-prepared nanocomposite can be best described by the pseudo-firstorder kinetics. The results are also in accordance with the high regression coefficients of 0.879, 0.924, and 0.785, respectively for pseudofirst-order owing to the closer predicted and experimental values. Whereas the reported overall low regression coefficients are 0.351, 0.938, and 0.621, respectively for pseudo-second-order. For a better understanding of the underlying adsorption processes involved, mainly due to the high adsorption capacity of the silica dispersion, the intraparticle diffusion model set forth by Weber and Morris was employed as well. According to the model's assumptions, a linear plot of the amount of adsorbent ($E1$ hormone) at time t (q_t) versus the square root of time indicates the existence of intraparticle diffusion. Moreover, if the graph plotted line passes through the origin at C = 0, then it indicates intraparticle diffusion is the rate-controlling step while in the case of C ≠0, some degree of boundary layer control is suggested [**67**]. As observed from **Fig. 7**d, the plot of Q_t vs $t^{0.5}$ appears to be linear for the sample in phase 1 but deviates slightly in the phase 2 segment of the plot. This indicates that both intraparticle diffusion and surface adsorption were contributing to the adsorption of $E1$ hormone onto the nanocomposite. Accordingly, a lower C value in the first phase suggests the contribution of intraparticle diffusion increased gradually with increasing time and then decreased in the second phase [**68**].

3.11. Isotherm modeling

In this study, two well-known adsorption isothermal models were also employed to elucidate the maximum adsorption capacity and to identify the adsorption processes [**69**]. Both isotherm models are valid for physical and chemical adsorption [**68**]. The isotherms were calculated using the following Langmuir (eqn. (**10**) and Freundlich (eqn. (**11**) equations and corresponding R^2 values for the models are given in **Table 6**.

$$\frac{C_e}{q_e} = \frac{1}{K_L Q_m} + \frac{C_e}{Q_m} \tag{10}$$

$$\ln q_e = \frac{1}{n} \ln C_e + \ln K_F \tag{11}$$

where C_e is the residual equilibrium hormone concentration (μg/L), Qm is the maximum adsorption capacity (μg/g), K_L is the Langmuir isotherm constant, K_F is the Freundlich constant, and n is the Freundlich heterogeneity factor. The obtained R^2 values for the Langmuir and Freundlich isotherms were 0.951 and 0.976, respectively, under the assumption that the adsorption of $E1$ hormone is monolayered chemisorption whereas multilayered for Freundlich. The maximum monolayer adsorption capacity was 230.9 μg/g while the separation factor values (R_L) in the range of 0.401-0.769 implied that the adsorption of $E1$ hormone was a favorable process. In the case of Freundlich model, K_F and 1/n values were 9.79 and 0.417 obtained, respectively. If the value of 1/n is between 0 and 1, then a favorable heterogeneous adsorption process is suggested on the surface of the adsorbent [**70**]. Moreover, a high correlation coefficient of 0.976 indicates a high adsorption affinity between the silica/g-C_3N_4 mesh and $E1$ hormone. From the obtained isotherms results (**Fig. 8**), it can be inferred that the nanocomposite possesses high adsorption capacity primarily due to silica as a support material.

3.12. Reusability and proposed degradation mechanism

From a practical viewpoint, it is imperative for any given photocatalyst to possess high stability and photoactivity under cyclic runs without suffering from any gradual loss in efficiency. The stability of the as-prepared nanocomposite was evaluated by subjecting it to concurrent cyclic runs. As can be seen in **Fig. 9**a, a degradation rate of 92.4% was observed for the first cyclic run while a robust photodegradation rate of over 75% was maintained even after seven cyclic runs. In the case of adsorption, a similar pattern is observed, with the highest adsorption of 26.5% for the first cycle which gradually decreased to around 6.5% for the 7th cycle. Although a minor reduction in both adsorption and photoactivity is observed, which can be attributed due to the loss of powered nanocomposite during the extraction of aliquots. Additionally, radical scavenging tests were also performed to elucidate possible degradation mechanisms.

Table 6 Calculated isotherm parameters for condition.

Langmuir model						
	Q_m (μg/g)	K_L (L/μg)	R_L	R^2	SSE	χ^2
Dark	230.94	2.98E-2	0.401 – 0.769	0.951	0.529	0.176
Freundlich model						
	K_F (μg/g)(L/μg)	n		R^2	SSE	χ^2
Dark	9.79	0.417		0.976	0.011	0.004

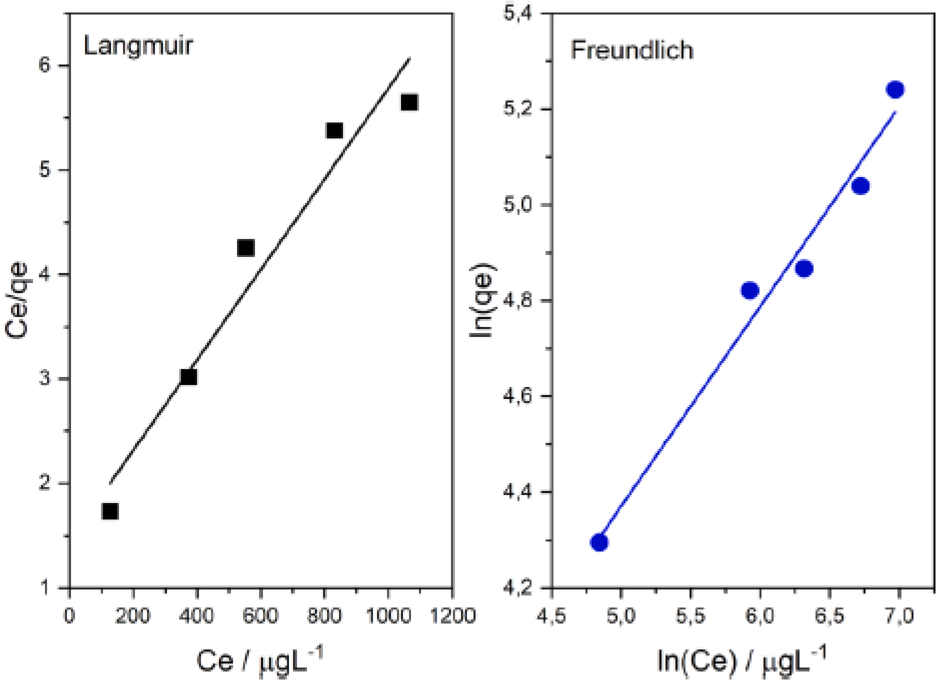

Fig. 8. Linear regression plots of Langmuir (left) and Freundlich isotherm (right) models for the removal of E1 hormone under dark condition.

In particular, p-benzoquinone (BQ), tert-butyl alcohol (TBA), and ethylenediaminetetraacetic acid (EDTA) were used for quenching $O_2^{\bullet-}$, $^\bullet$OH, and h^+ charged species, respectively. From **Fig. 9**b, it can be seen that compared to the control sample, the addition of trapping agents led to a decrease in the photoactivity, indicating at all charged species were involved in the degradation except TBA. However, the highest reduction in the photoactivity was observed for the BQ, suggesting the dominant degradation occurred via the reductive pathway of $O_2^{\bullet-}$. The order of degree for the primary contribution of radical species can be inferred as $O_2^{\bullet-} > h^+ >$ $^\bullet$OH, which is in accordance with the data reported in the literature for the same photocatalyst [**71**]. Based on the results, it can be deduced that the photocatalytic degradation of $E1$ hormone is primarily due to the presence of superoxide anion, which attacks $E1$ hormone as well as the minor contribution from the oxidation pathway of holes as depicted in **Fig. 9**c. Interestingly, the degradation pathway of $E1$ appears to be different from the hydroxylation, the proposed mechanism in the case of TiO_2 [**72**], indicating that the production of both reducing and oxidizing species generated by the nanocomposite was beneficial for the degradation process. Additionally, in order to further substantiate the photocatalytic degradation mechanism, $LCMS$ analysis was carried out from the irradiated sample evaluated using optimized parameters under visible light. $LCMS$ results indicated that the parent $E1$ hormone (m/z = 269.0973) was fragmented into different degradation product ions and are identified as having m/z ratios of 183.0183, 159.0276, and 145.0098.

3.13. Photocatalytic antibacterial activity

The antibacterial properties of the as-prepared nanocomposite were evaluated against the gram-positive and gram-negative bacteria as shown in **Fig. 10**. As can be seen, the as-prepared nanocomposite exhibits superior antibacterial activity against the gram-positive S. aureus as no bacterial growth was observed after 1 h of UV-vis light irradiation. Moreover, the reference sample under dark test conditions also exhibited reduced bacterial growth. In the case of gram-negative, $E.coli$, the antibacterial activity was greatly reduced in comparison to the grampositive; nonetheless, significant antibacterial was observed under both UV and visible light irradiation. Interestingly, the as-prepared nanocomposite possessed significant antibacterial performance under blank conditions, indicating that the as-prepared material might have intrinsic properties for bacterial growth inhibition. The bactericidal properties of g-C_3N_4 under dark test are attributed to the intrinsic electrostatic attraction between the porous structure and lipid heads [**73**]. The calculated antibacterial activities are given in **Table 7**.

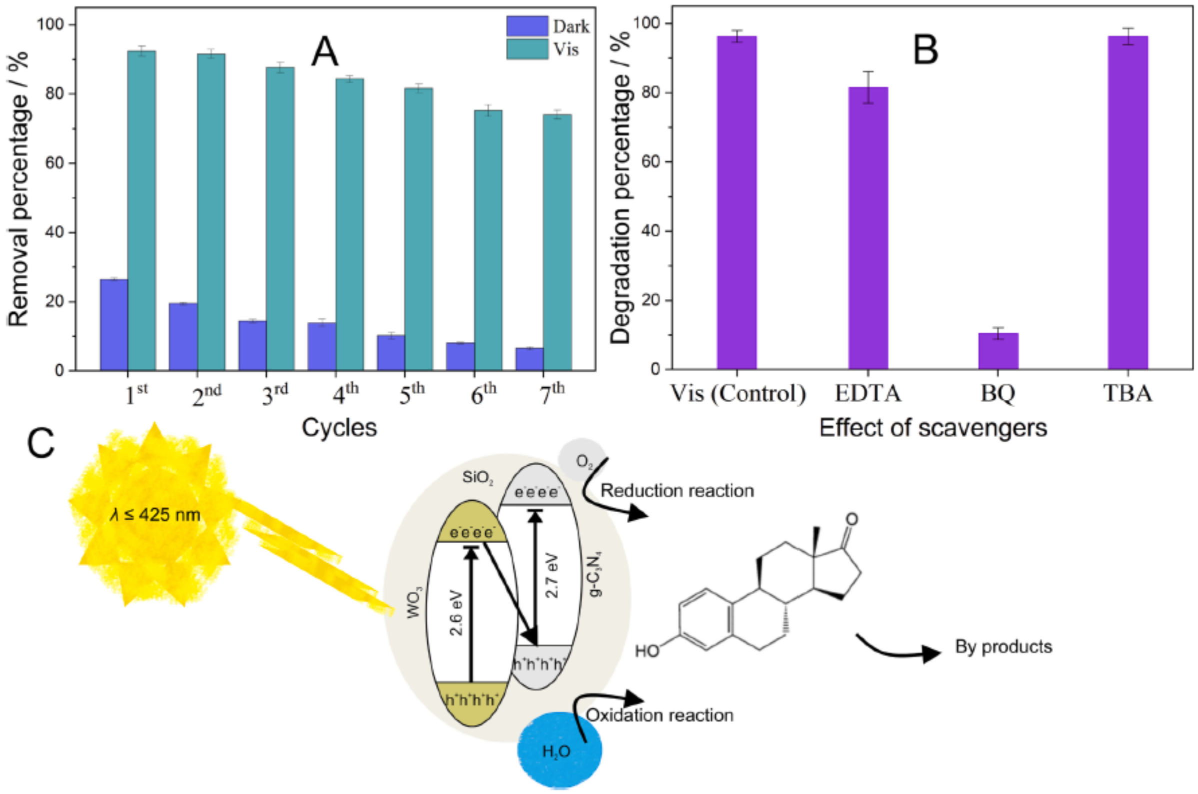

Fig. 9. Reusability study (a), radical quenching tests effect on photocatalytic degradation (b), and photo-degradation mechanism of $E1$ hormone (c).

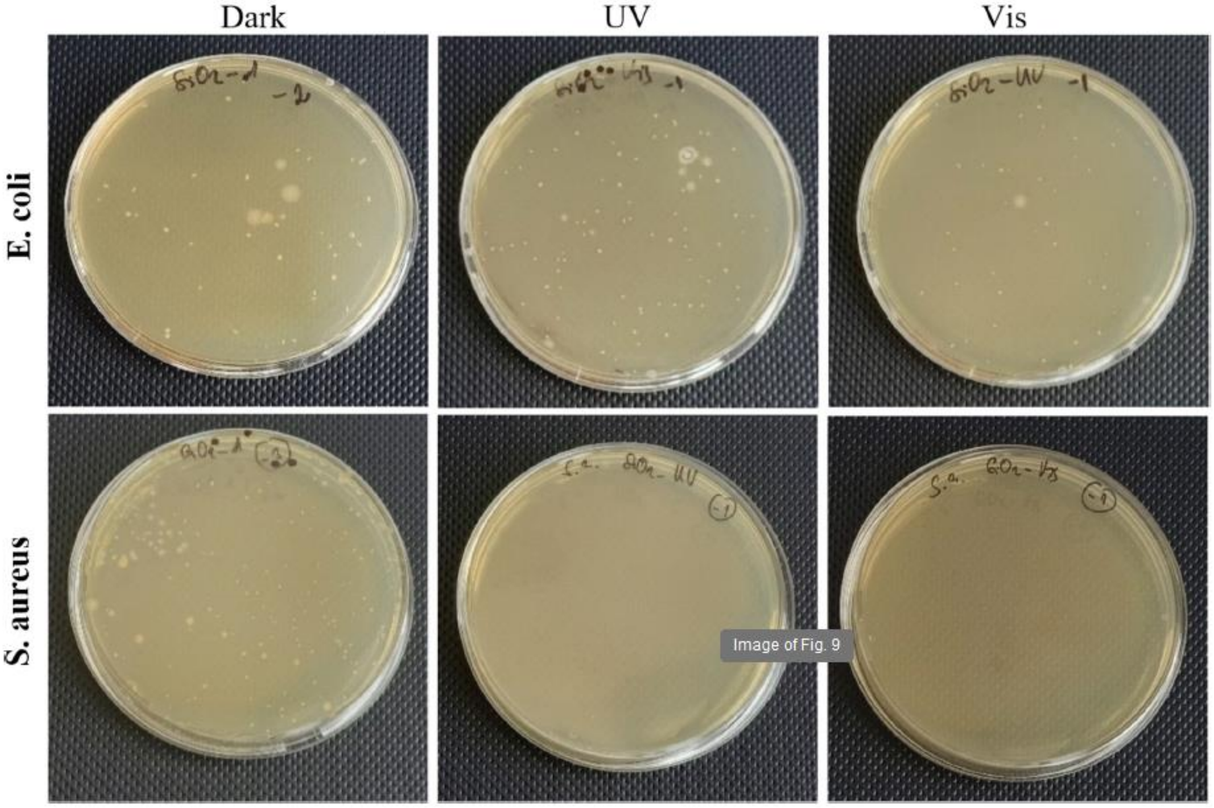

Fig. 10. Bacterial colonies formation after dark, UV, and visible light irradiation.

Table 7 Calculated antibacterial activity of the as-prepared nanocomposite.

Sample		Bacteria			
		Escherichia coli		*Staphylococcus aureus*	
		Initial conc. of bacteria (CFU/mL)	Bacterial conc. After 24 h incubation	Initial conc. of bacteria (CFU/mL)	Bacterial conc. After 24 h incubation
Silica-supported g–C_3N_4/ WO_3	Dark	6.0×10^6	4.0×10^3	6.0x10^6	1.87×10^5
	UV		4.8×10^2		No growth
	Vis		9.3×10^2		No growth

4. Conclusions

In this study, we applied the response surface methodology based on the Box-Behnken design for the photocatalytic degradation of estrone ($E1$) hormone under UV and visible light irradiation using silica-supported g-C_3N_4/WO_3. The observed experimental and predicted data suggest the developed model is suitable for second-order polynomial response equation and analysis of variance, with a high degree of coefficient of determination ($R^2 > 0.958$ and 0.934 for UV and visible, respectively) for photocatalytic degradation. The predicted and experimental values were also close to each with a high degree of certainty. The optimized process parameters were found to be as follows: 3000 μg of photocatalyst dosage, pH 7, and 300 μg/L hormone concentration. Under these experimental conditions, the photocatalytic degradation of $E1$ hormone was observed to be about 100.0% and

96.2% using UV and visible light irradiation, respectively. Moreover, the stability of the photocatalyst was also tested in a consecutive seven-cyclic study which demonstrated that the photocatalyst was able to maintain robust photoactivity above 75% even after several repeated cyclic runs. Additionally, the prepared photocatalyst was found to have significant antibacterial activity against both gram-positive and gram-negative bacteria. These results indicate that the optimization of photocatalytic process parameters of silica-supported g-C_3N_4/WO_3 using the Box-Behnken model approach is highly suitable for targeting persistent environmental pollutants.

References

[1] T. Teymourian, T. Teymoorian, E. Kowsari, S. Ramakrishna, A review of emerging PFAS contaminants: sources, fate, health risks, and a comprehensive assortment of recent sorbents for PFAS treatment by evaluating their mechanism, Res. Chem. Intermed. 47 (2021) 4879-4914, **https://doi.org/10.1007/S11164-021-04603-7**.

[2] V.L. Marlatt, S. Bayen, D. Castaneda-Cortes, G. Delbes, P. Grigorova, V.S. Langlois, C.J. Martyniuk, C.D. Metcalfe, L. Parent, A. Rwigemera, et al., Impacts of endocrine disrupting chemicals on reproduction in wildlife and humans, Environ. Res. 208 (2022), 112584, **https://doi.org/10.1016/J.ENVRES.2021.112584**.

[3] S. Antony, S. Antony, S. Rebello, S. George, D.T. Biju, A. Madhavan, P. Binod, A. Pandey, R. Sindhu, et al., Bioremediation of endocrine disrupting chemicals-advancements and challenges, Environ. Res. 213 (2022), 113509, **https://doi.org/ 10.1016/J.ENVRES.2022.113509**.

[4] F. Egalini, L. Marinelli, M. Rossi, G. Motta, N. Prencipe, R. Rossetto Giaccherino, L. Pagano, S. Grottoli, R. Giordano, Endocrine disrupting chemicals: effects on pituitary, thyroid and adrenal glands, Endocrine 2022 (2022) 1-11, **https://doi. org/10.1007/S12020-022-03076-X**.

[5] New EU Criteria for Endocrine Disrupters. 2018, 10.6027/TN2018-537.

[6] T. Jin, M. Peydayesh, H. Joerss, J. Zhou, S. Bolisetty, R. Mezzenga, Amyloid fibril-based membranes for PFAS removal from water, Environ. Sci. (Camb) 7 (2021) 1873-1884, **https://doi.org/10.1039/D1EW00373A**.

[7] E.W. Tow, M.S. Ersan, S. Kum, T. Lee, T.F. Speth, C. Owen, C. Bellona, M. N. Nadagouda, A.M. Mikelonis, P. Westerhoff, et al., Managing and treating per-and polyfluoroalkyl substances (PFAS) in membrane concentrates, AWWA Water. Sci. 3 (2021) e1233.

[8] D. Leonello, M.A. Fendrich, F. Parrino, N. Patel, M. Orlandi, A. Miotello, Light-induced advanced oxidation processes as PFAS remediation methods: a review, Appl. Sci. 11 (2021) 8458, **https://doi.org/10.3390/APP11188458**.

[9] X. Yao, J. Zuo, Y.J. Wang, N.N. Song, H.H. Li, K. Qiu, Enhanced photocatalytic degradation of perfluorooctanoic acid by mesoporous Sb2O3/TiO2 heterojunctions, Front. Chem. 9 (2021) 352, **https://doi.org/10.3389/ FCHEM.2021.690520**.

[10] S. Tabatabaei, S. Dastmalchi, A. Mehrizad, P. Gharbani, Enhancement of 4-nitro-phenol ozonation in water by nano ZnO catalyst, J. Environ. Health. Sci. Eng. 8 (2011) 363-372.

[11] M. Bodzek, Nanoparticles for water disinfection by photocatalysis: a review, Arch. Environ. Prot. 48 (3-17) (2022), **https://doi.org/10.24425/AEP.2022.140541**.

[12] A. Purabgola, N. Mayilswamy, B. Kandasubramanian, Graphene-based TiO2 composites for photocatalysis & environmental remediation: synthesis and progress, Environ. Sci. Pollut. Res. 29 (2022) 32305-32325, **https://doi.org/ 10.1007/S11356-022-18983-9**.

[13] L. Hu, R. Wang, M. Wang, Y. Xu, C. Wang, Y. Liu, J. Chen, Research progress of photocatalysis for algae killing and inhibition: a review, Environ. Sci. Pollut. Res. 29 (2022) 47902-47914, **https://doi.org/10.1007/S11356-022-20645-9**.

[14] P. Kajitvichyanukul, V.H. Nguyen, T. Boonupara, L.A. Phan Thi, A. Watcharenwong, S. Sumitsawan, P. Udomkun, Challenges and effectiveness of nanotechnology-based photocatalysis for pesticides-contaminated water: a review, Environ Res 212 (2022), 113336, **https://doi.org/10.1016/J. ENVRES.2022.113336**.

[15] V. Verma, M. Al-Dossari, J. Singh, M. Rawat, M.G.M. Kordy, M. Shaban, A review on green synthesis of tio2 nps: photocatalysis and antimicrobial applications, Polymers 14 (2022) 1444, **https://doi.org/10.3390/POLYM14071444**.

[16] A.B. Djurisic, Y. He, A.M.C. Ng, Visible-light photocatalysts: prospects and challenges, APL Mater. 8 (2020), 030903, **https://doi.org/10.1063/L5140497**.

[17] C. Li, J. Li, Y. Huang, J. Liu, M. Ma, K. Liu, C. Zhao, Z. Wang, S. Qu, L. Zhang, et al., Recent development in electronic structure tuning of graphitic carbon nitride for highly efficient photocatalysis, J. Semicond. 43 (2022), **https://doi.org/10.1088/ 1674-4926/43/2/021701**.

[18] S. Swetha, B. Janani, S.S. Khan, A critical review on the development of metal-organic frameworks for boosting photocatalysis in the fields of energy and environment, J. Clean Prod. 333 (2022), 130164, **https://doi.org/10.1016/J. JCLEPRO.2021.130164**.

[19] R. Pelosato, I. Bolognino, F. Fontana, I.N. Sora, Applications of heterogeneous photocatalysis to the degradation of oxytetracycline in water: a review, Molecules (2022) 27, **https://doi.org/10.3390/MOLECULES27092743**.

[20] A. Akhundi, A. Zaker Moshfegh, A. Habibi-Yangjeh, M. Sillanpaa, Simultaneous dual-functional photocatalysis by g-C 3 N 4 -based nanostructures, ACS ES&T Eng 2 (2022) 564-585, **https://doi.org/10.1021/ACSESTENGG.1C00346**.

[21] P. Kumari, N. Bahadur, L. Kong, L.A. O'Dell, A. Merenda, L.F. Dumee, Engineering Schottky-like and heterojunction materials for enhanced photocatalysis performance - a review, Mater. Adv. 3 (2022) 2309-2323, **https://doi.org/ 10.1039/D1MA01062J**.

[22] Y. Nosaka, A.Y. Nosaka, Generation and detection of reactive oxygen species in photocatalysis, Chem. Rev. 117 (2017) 11302-11336, **https://doi.org/10.1021/ acs.chemrev.7b00161**.

[23] R. Mutsak Ahmed, I. Hasan, A review on properties and applications of TiO2 and associated nanocomposite materials, Mater. Today Proc. (2021), **https://doi.org/ 10.1016/j.matpr.2021.04.381**.

[24] H. Liu, J. Feng, W. Jie, A review of noble metal (Pd, Ag, Pt, Au)-zinc oxide nanocomposites: synthesis, structures and applications, J. Mater. Sci.: Mater. Electron. 28 (2017) 16585-16597, **https://doi.org/10.1007/s10854-017-7612-0**.

[25] H. Ali, A. Guler, M. Masar, P. Urbanek, M. Urbanek, D. Skoda, P. Suly, M. Machovsky, D. Galusek, I. Kuritka, Solid-state synthesis of direct Z-scheme Cu2O/WO3 nanocomposites with

enhanced visible-light photocatalytic performance, Catalysts 11 (2021) 293, **https://doi.org/10.3390/catal11020293**.

[26] S. Das, T. Deka, P. Ningthoukhangjam, A. Chowdhury, R.G. Nair, A critical review on prospects and challenges of metal-oxide embedded g-C3N4-based direct Z-scheme photocatalysts for water splitting and environmental remediation, Appl. Surf. Sci. Adv. 11 (2022), 100273, **https://doi.org/10.1016/J. APSADV.2022.100273**.

[27] J.C. Murillo-Sierra, A. Hernandez-Ramirez, L. Hinojosa-Reyes, J.L. Guzman-Mar, A review on the development of visible light-responsive WO3-based photocatalysts for environmental applications, Chem. Eng. J. Adv. 5 (2021), 100070, **https://doi. org/10.1016/J.CEJA.2020.100070**.

[28] Y.H. Nien, C.K. Li, Y.L. Lin, Preparation of ultrafine fibrous membranes containing graphitic carbon nitride composited photocatalyst and their degradation of methylene blue under visible light, J. Poly. Res. 28 (2021) 1-11, **https://doi.org/ 10.1007/S10965-021-02829-Y**.

[29] M. Huang, C. Chen, T. Wang, Q. Sui, K. Zhang, B. Li, Cadmium-sulfide/gold/ graphitic-carbon-nitride sandwich heterojunction photocatalyst with regulated electron transfer for boosting carbon-dioxide reduction to hydrocarbon, J. Colloid Interface Sci. 613 (2022) 575-586, **https://doi.org/10.1016/JCIS.2022.01.065**.

[30] F. Wang, W. Li, W. Zhang, R. Ye, X. Tan, Facile fabrication of the Ag nanoparticles decorated graphitic carbon nitride photocatalyst film for indoor air purification under visible light, Build. Environ. 222 (2022), 109402, **https://doi.org/10.1016/ J.BUILDENV.2022.109402**.

[31] O. Altan, E. Altintas, S. Alemdar, O. Metin, The rational design of a graphitic carbon nitride-based dual S-scheme heterojunction with energy storage ability as a day/night photocatalyst for formic acid dehydrogenation, Chem. Eng. J. 441 (2022), **https://doi.org/10.1016ZJ.CEJ.2022.136047**.

[32] J.K. George, A. Bhagat, B. Bhaduri, N. Verma, Carbon nanofiber-bridged carbon nitride-Fe2O3 photocatalyst: hydrogen generation and degradation of aqueous organics, Catal. Lett. (2022), **https://doi.org/10.1007/S10562-022-03985-6**.

[33] R. Gusain, N. Kumar, S.S. Ray, Factors influencing the photocatalytic activity of photocatalysts in wastewater treatment, Photocatal Adv Oxid Process Wastewater Treat. 229-270 (2020), **https://doi.org/10.1002/9781119631422.CH8**.

[34] S.A. Mosavi, A. Ghadi, P. Gharbani, A. Mehrizad, Photocatalytic removal of methylene blue using Ag@CdSe/Zeoilte nanocomposite under visible light irradiation by response surface methodology, Mater. Chem. Phys. 267 (2021), 124696, **https://doi.org/10.1016/J.MATCHEMPHYS.2021.124696**.

[35] S. Baghbani Ghatar, S. Allahyari, N. Rahemi, M. Tasbihi, Response surface methodology optimization for photodegradation of methylene blue in a ZnO coated flat plate continuous photoreactor, Int. J. Chem React. Eng. 16 (2018), **https://doi. org/10.1515/ijcre-2017-0221**.

[36] H. Dadkhah, M.A. Behnajady, Optimization of Photooxidative Removal of P-Nitrophenol in a Spinning Disc Photoreactor Using Response Surface Methodology. 2018, 206, 398-408, 10.1080/00986445.2018.1494581.

[37] H.E. Okten, A Box-Behnken Design (BBD) optimization of the photocatalytic degradation of 2,4-dichlorophenoxyacetic acid (2,4-D), Using TiO. (2018), **https://doi.org/10.5004/dwt.2018.22681**.

[38] M.P. Mazhari, M. Hamadanian, M. Mehipour, V. Jabbari, Central composite design (CCD) optimized synthesis of Fe3O4@SiO2@AgCl/Ag/Ag2S as a novel magnetic nano-photocatalyst for catalytic degradation of organic pollutants, J. Environ. Chem. Eng. 6 (2018) 7284-7293, **https://doi.org/10.1016/JJECE.2018.11.024**.

[39] P. Taghizadeh-Lendeh, A.H.M. Sarrafi, A. Alihosseini, N. Bahri-Laleh, Degradation of methyldiethanolamine and gas refinery effluent using a TiO2@WO3/ZnO photocatalyst: central composite design optimization, New J. Chem. (2022), **https://doi.org/10.1039/D2NJ03769F**.

[40] **B.B. Garcia, G. Lourinho, P. Romano, P.S.D. Brito, Photocatalytic degradation of swine wastewater on aqueous TiO2 suspensions: optimization and modeling via Box-Behnken design, Heliyon 6 (2020) e03293**.

[41] Tetteh, E.K.; Rathilal, S. Response surface optimization of biophotocatalytic degradation of industrial wastewater for bioenergy recovery. Bioeng. 2022, 9, 95, 10.3390/BIOENGINEERING9030095.

[42] M. Bagal, G. Kumbhar, S. Shukla, A. Tiwari, D. Gajbhiye, A. Mohod, Degradation of dye in a continuous zig-zag flow pattern photocatalytic reactor using a Doehlert matrix, Chem. Eng. Res. Des. (2022), **https://doi.org/10.1016/J.CHERD.2022.09.019**.

[43] K. Ahmad, H.R. Ghatak, S.M. Ahuja, Response surface methodology (RSM) and artificial neural network (ANN) approach to optimize the photocatalytic conversion of rice straw hydrolysis residue (RSHR) into vanillin and 4-hydroxybenzaldehyde, Chem. Prod. Process Model. (2022), **https://doi.org/ 10.1515/CPPM-2022-0003**.

[44] N. Mohammed, P. Palaniandy, F. Shaik, Solar photocatalytic biodegradability of saline water: optimization using RSM and ANN, AIP Conf. Proc. 2463 (2022), 020027, **https://doi.org/10.1063/5.0080297**.

[45] A. Mehrizad, P. Gharbani, Application of central composite design and artificial neural network in modeling of reactive blue 21 dye removal by photo-ozonation process, Water Sci. Tech. 74 (2016) 184-193, **https://doi.org/10.2166/ WST.2016.199**.

[46] M.N. Chollom, S. Rathilal, F.M. Swalaha, B.F. Bakare, E.K. Tetteh, Comparison of response surface methods for the optimization of an upflow anaerobic sludge blanket for the treatment of slaughterhouse wastewater, Environ. Eng. Res. 25 (2020) 114-122, **https://doi.org/10.4491/EER.2018.366**.

[47] W.K. Jo, R.J. Tayade, New generation energy-efficient light source for photocatalysis: LEDs for environmental applications, Ind. Eng. Chem. Res. 53 (2014) 2073-2084, **https://doi.org/10.1021/IE404176G**.

[48] M. Yasir, T. Sopik, L. Lovecka, D. Kimmer, V. Sedlarik, The adsorption, kinetics, and interaction mechanisms of various types of estrogen on electrospun polymeric nanofiber membranes, Nanotechnol. 33 (2021), 075702, **https://doi.org/10.1088/ 1361-6528/AC357B**.

[49] J. Guo, J. Zhou, Z. Sun, M. Wang, X. Zou, H. Mao, F. Yan, Enhanced photocatalytic and antibacterial activity of acridinium-grafted g-C3N4 with broad-spectrum light absorption for antimicrobial photocatalytic therapy, Acta Biomater. 146 (2022) 370-384, **https://doi.org/10.1016/J.ACTBIO.2022.03.052**.

[50] J. Sun, Z. Xu, W. Li, X. Shen, Effect OF nano-SiO2 on the early hydration of alite-sulphoaluminate cement, Nanomater. 7 (2017) 102, **https://doi.org/10.3390/ NANO7050102**.

[51] S. Sun, C. Li, Z. Sun, J. Wang, X. Wang, H. Ding, In-situ design of efficient hydroxylated SiO2/g-C3N4 composite photocatalyst: synergistic effect of compounding and surface hydroxylation, Chem. Eng. J. 416 (2021), 129107, **https://doi.org/10.1016/J.CEJ.2021.129107**.

[52] C. Ding, Q. Zhu, B. Yang, E. Petropoulos, L. Xue, Y. Feng, S. He, L. Yang, Efficient photocatalysis of tetracycline hydrochloride (TC-HCl) from pharmaceutical wastewater using AgCl/ZnO/g-C3N4 composite under visible light: process and mechanisms, J. Environ. Sci. 126 (2023) 249-262, **https://doi.org/10.1016/J. JES.2022.02.032**.

[53] M. Esmati, A. Allahresani, A. Naghizadeh, Synthesis and characterization of Graphitic Carbon Nitride/Mesoporous Nano-Silica (g-C3N4/KCC-1) nanocomposite as a novel highly efficient and recyclable photocatalyst for degradation of antibiotic in aqueous solution, Res. Chem. Intermed. 47 (4) (2021) 1447-1469, **https://doi.org/10.1007/S11164-020-04358-7**.

[54] T. Ohno, N. Murakami, T. Koyanagi, Y. Yang, Photocatalytic reduction of CO2 over a hybrid photocatalyst composed of WO3 and graphitic carbon nitride (g-C3N4) under visible light, J. CO2 Util. 6 (2014) 17-25, **https://doi.org/10.1016/J. JCOU.2014.02.002**.

[55] I. Aslam, C. Cao, M. Tanveer, W.S. Khan, M. Tahir, M. Abid, F. Idrees, F.K. Butt, Z. Ali, N. Mahmood, The synergistic effect between WO3 and G-C3N4 towards efficient visible-light-driven photocatalytic performance, New J. Chem. 38 (2014) 5462-5469, **https://doi.org/10.1039/C4NJ01370K**.

[56] Y. Tao, O. de Luca, B. Singh, A.J. Kamphuis, J. Chen, P. Rudolf, P.P. Pescarmona, WO3-SiO2 nanomaterials synthesized using a novel template-free method in supercritical CO2 as heterogeneous catalysts for epoxidation with H2O2, Mater. Today Chem. 18 (2020), 100373, **https://doi.org/10.1016/J. MTCHEM.2020.100373**.

[57] A. Allahresani, M.A. Nasseri, A. Nakhaei, SiO2/g-C3N4 nanocomposite-catalyzed green synthesis of di-indolyloxindols under mild conditions, Res. Chem. Intermed. 43 (2017) 6367-6378, **https://doi.org/10.1007/S11164-017-2994-4**.

[58] N. Djohan, N. Sevani, R. Estrada, H. Hardhienata, Irzaman, The Optical Band Gap Based on K-M Function on Layer of LiTaO3 with Variation Treatment of Annealing Temperature. 2018 International Conference on Smart Green Technology in Electrical and Information Systems: Smart Green Technology for Sustainable Living, ICSGTEIS 2018 - Proceeding 2018, 35-38, 10.1109/ICSGTEIS.2018.8709111.

[59] F. Ambroz, T.J. Macdonald, V. Martis, I.P. Parkin, F. Ambroz, T.J. Macdonald, I. P. Parkin, V. Martis, Evaluation of the BET theory for the characterization of meso and microporous MOFs, Small Methods 2 (2018) 1800173, **https://doi.org/ 10.1002/SMTD.201800173**.

[60] M. Thommes, K. Kaneko, A. Neimark, J.P. Olivier, F. Rodriguez-Reinoso, J. Rouquerol, K.S.W. Sing, Physisorption of gases, with special reference to the evaluation of surface area and pore

size distribution (IUPAC Technical Report), Pure Appl. Chem. 87 (2015) 1051-1069, **https://doi.org/10.1515/PAC-2014-1117**.

[61] J. Han, W. Qiu, W. Gao, Adsorption of estrone in microfiltration membrane filters, Chem. Eng. J. 165 (2010) 819-826, **https://doi.org/10.1016/J.CEJ.2010.10.024**.

[62] Abdel-Gawad, S.A.; Hossam, •; Abdel-Aziz, M. Removal of ethinylestradiol by adsorption process from aqueous solutions using entrapped activated carbon in alginate biopolymer: isotherm and statistical studies. Appl. Water Sci. 2019 9:4 2019, 9, 1-8, 10.1007/S13201-019-0951-7.

[63] L.A. Al-Khateeb, A.Y. Obaid, N.A. Asiri, M. Abdel Salam, Adsorption behavior of estrogenic compounds on carbon nanotubes from aqueous solutions: kinetic and thermodynamic studies, J. Ind. Eng. Chem. 20 (2014) 916-924, **https://doi.org/ 10.1016/J.JIEC.2013.06.023**.

[64] E.N. Bakatula, D. Richard, C.M. Neculita, G.J. Zagury, Determination of point of zero charge of natural organic materials, Environ. Sci. Pollut. Res. 25 (2018) 7823-7833, **https://doi.org/10.1007/S11356-017-1115-7**.

[65] F. Esmaeeli, S.A. Gorbanian, N. Moazezi, Removal of estradiol valerate and progesterone using powdered and granular activated carbon from aqueous solutions, Int. J. Environ. Res. 11 (2017) 695-705, **https://doi.org/10.1007/ S41742-017-0060-0**.

[66] A. Mehrizad, P. Gharbani, Novel ZnS/carbon nanofiber photocatalyst for degradation of rhodamine 6G: kinetics tracking of operational parameters and development of a kinetics model, Photochem. Photobiol. 93 (2017) 1178-1186, **https://doi.org/10.1111/PHP.12795**.

[67] Kurajica, S.; Minga, I.; Blazic, R.; Muzina, K.; Tominac, P. Adsorption and degradation kinetics of methylene blue on as-prepared and calcined titanate nanotubes. Athens J. Sci. 5, 10.30958/ajs.5-1-1.

[68] H. Guo, Y. Ke, D. Wang, K. Lin, R. Shen, J. Chen, W. Weng, Efficient adsorption and photocatalytic degradation of congo red onto hydrothermally synthesized NiS nanoparticles, J. Nanopart. Res. 15 (2013) 1-12, **https://doi.org/10.1007/S11051-013-1475-Y**.

[69] Mehrizad, A.; Gharbani, P. Decontamination of 4-chloro-2-nitrophenol from aqueous solution by graphene adsorption: equilibrium, kinetic, and thermodynamic studies. Pol J. Environ. Stud. 2014, 23, 2111-2116, 10.15244/PJOES/26779.

[70] Andronic, L.; Isac, L.; Cazan, C.; Enesca, A. Simultaneous adsorption and photocatalysis processes based on ternary TiO2-CuxS-fly ash hetero-structures. Appl. Sci. 2020, Vol. 10, Page 8070 2020, 10, 8070, 10.3390/APP10228070.

[71] Y. Yang, B. Liu, J. Xu, Q. Wang, X. Wang, G. Lv, J. Zhou, The synthesis of H-BN-modified Z-scheme WO3/g-C3N4 heterojunctions for enhancing visible light photocatalytic degradation of tetracycline pollutants, ACS Omega 7 (2022) 6035-6045, **https://doi.org/10.1021/ACSOMEGA.1C06377**.

[72] R.N. Padovan, L.S. de Carvalho, P.L. de Souza Bergo, C. Xavier, A. Leitâo, A .J. dos Santos Neto, F.M. Lanças, E.B. Azevedo, Degradation of hormones in tap water by heterogeneous solar TiO2-photocatalysis: optimization, degradation products identification, and estrogenic activity

removal, J. Environ Chem. Eng. 9 (2021), 106442, **https://doi.org/10.1016/JJECE.2021.106442**.

[73] H. Cui, Z. Gu, X. Chen, L. Lin, Z. Wang, X. Dai, Z. Yang, L. Liu, R. Zhou, M. Dong, Stimulating antibacterial activities of graphitic carbon nitride nanosheets with plasma treatment, Nanoscale 11 (2019) 18416-18425, **https://doi.org/10.1039/ C9NR03797G**.